Remote Sensing of Environment xxx (xxxx) xxx–xxx

Contents lists available at ScienceDirect

Remote Sensing of Environment

journal homepage: www.elsevier.com/locate/rse

Tracking annual changes of coastal tidal flats in China during 1986–2016 through analyses of Landsat images with Google Earth Engine

Xinxin Wang[a], Xiangming Xiao[b,*], Zhenhua Zou[b], Bangqian Chen[c], Jun Ma[a], Jinwei Dong[d], Russell B. Doughty[b], Qiaoyan Zhong[a], Yuanwei Qin[b], Shengqi Dai[a], Xiangping Li[a], Bin Zhao[a], Bo Li[a]

[a] Ministry of Education Key Laboratory of Biodiversity Science and Ecological Engineering, Institute of Biodiversity Science, Fudan University, Shanghai 200433, China
[b] Department of Microbiology and Plant Biology, Center for Spatial Analysis, University of Oklahoma, Norman, OK 73019, USA
[c] Rubber Research Institute (RRI), Chinese Academy of Tropical Agricultural Sciences (CATAS), Hainan Province 571737, China
[d] Key Laboratory of Land Surface Pattern and Simulation, Institute of Geographic Sciences and Natural Resources Research, Chinese Academy of Sciences, Beijing 100101, China

ARTICLE INFO

Keywords:
Tidal flats
Time series Landsat images
Pixel and frequency-based algorithm
Google Earth Engine
China coastal zone

ABSTRACT

Tidal flats (non-vegetated area), along with coastal vegetation area, constitute the coastal wetlands (intertidal zone) between high and low water lines, and play an important role in wildlife, biodiversity and biogeochemical cycles. However, accurate annual maps of coastal tidal flats over the last few decades are unavailable and their spatio-temporal changes in China are unknown. In this study, we analyzed all the available Landsat TM/ETM + /OLI imagery (~44,528 images) using the Google Earth Engine (GEE) cloud computing platform and a robust decision tree algorithm to generate annual frequency maps of open surface water body and vegetation to produce annual maps of coastal tidal flats in eastern China from 1986 to 2016 at 30-m spatial resolution. The resulting map of coastal tidal flats in 2016 was evaluated using very high-resolution images available in Google Earth. The total area of coastal tidal flats in China in 2016 was about 731,170 ha, mostly distributed in the provinces around Yellow River Delta and Pearl River Delta. The interannual dynamics of coastal tidal flats area in China over the last three decades can be divided into three periods: a stable period during 1986–1992, an increasing period during 1993–2001 and a decreasing period during 2002–2016. The resulting annual coastal tidal flats maps could be used to support sustainable coastal zone management policies that preserve coastal ecosystem services and biodiversity in China.

1. Introduction

Coastal wetlands are usually composed of coastal vegetation area and tidal flats (or intertidal flats, often referred as coastal non-vegetated areas). Coastal tidal flats often include mud flats, sand, and rocky areas (Fig. 1) (Dyer et al., 2000), and are natural transitions from terrestrial ecosystems to ocean ecosystems (Kline and Swallow, 1998; Oost et al., 2012; Wei et al., 2015; Yao, 2013). They also serve as critical wildlife habitat for large populations of waterfowl and migratory birds (e.g., Great Knot), crabs, mollusks, and fish (Barbier et al., 2008; Ghosh et al., 2016; Koch et al., 2009; Ma and Li, 2015). Furthermore, tidal flats prevent coastal erosion and serve as buffer zones that help protect inland communities from storms and other natural hazards (Jin et al., 2017; Murray et al., 2014).

However, tidal flats are one of the most vulnerable areas on Earth due to anthropogenic activities and natural disturbances, such as global warming induced sea-level rise (Blum and Roberts, 2009; Kolker et al., 2011; Morris et al., 2002; Rodriguez et al., 2017), coastal erosion, land reclamation (Feng et al., 2012; Wei et al., 2015), aquaculture, salterns, impoundments, and diversions (Ma et al., 2014; Syvitski et al., 2005). For example, approximately 16 km^2 of coastal tidal flats were destroyed in the Ariake Bay in the early 1990s in Japan (Hodoki and Murakami, 2006). The preservation of tidal flats depends on our ability to accurately monitor their spatial distribution and temporal variations (Zahran et al., 2006).

Many global land cover data products have a wetland layer, such as the 1-km International Geosphere-Biosphere Programme Data and Information System Cover (IGBP-DISCover) map (Loveland et al., 2000), the 1-km University of Maryland (UMD) land-cover map (Hansen et al., 2000), the 1-km Global Land Cover 2000 (GLC2000)

* Corresponding author at: Department of Microbiology and Plant Biology, University of Oklahoma, Norman, OK 73019, USA.
E-mail address: xiangming.xiao@ou.edu (X. Xiao).

https://doi.org/10.1016/j.rse.2018.11.030
Received 11 July 2018; Received in revised form 10 November 2018; Accepted 21 November 2018

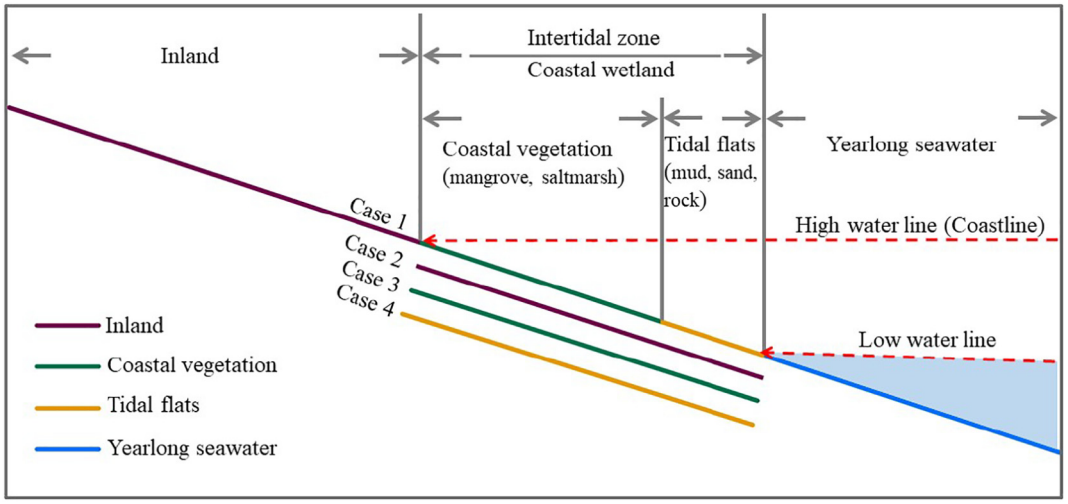

Fig. 1. An illustration of inland, wetland distribution (coastal vegetation, tidal flats) and yearlong sea water. Case1: Common classification system for wetlands, including both coastal vegetation and tidal flats; Case 2: There is no intertidal zone between inland and yearlong seawater; Case 3: There are no barren tidal flats but only coastal vegetation in the intertidal zone; Case 4: There are no coastal vegetation but only tidal flats in the intertidal zone.

map (Bartholome and Belward, 2005), the 500-m Moderate Resolution Imaging Spectrometer (MODIS) land-cover maps (Friedl et al., 2010; Friedl et al., 2002), the 300-m GlobCover land-cover maps (Arino et al., 2008), and the 30-m global land cover map generated using Landsat TM and ETM + data under the Fine Resolution Observation and Monitoring of Global Land Cover (FROM-GLC) project (Gong et al., 2013). However, these land cover data products have different classification systems, and do not include a layer for coastal tidal flats and information on the annual spatial distribution of tidal flats in China. In addition, a number of research projects have focused on wetland classification (Chen et al., 2016; Gong et al., 2010; Niu et al., 2009, 2012), including tidal flats monitoring at regional (Dyer et al., 2000; Gade et al., 2008; Ghosh et al., 2016; Liu et al., 2013; Mason et al., 2010; Murray et al., 2014; Ryu et al., 2002; Wang and Niu, 2017; Wei et al., 2015; White and Madsen, 2016; Zhao et al., 2008) and national scales (Dhanjal-Adams et al., 2016; Murray et al., 2012; Sagar et al., 2017; Tseng et al., 2017). However, most of those studies did not explicitly differentiate coastal vegetation area and coastal tidal flats (Liu et al., 2013; Murray et al., 2014; Sagar et al., 2017; Wang and Niu, 2017). A recent study mapped coastal tidal flats in the Yangstze Estuary using all Landsat images within 5 years windows through visual interpretation method (Chen et al., 2016). Therefore, there are no annual maps of coastal tidal flats in China since mid-1980s at a relative high spatial resolution, which could be used to illustrate the annual dynamics of tidal flat areas and assess the impacts of socio-economic developments since 1980s on the coastal zones in China. It's imperative for us to develop annual maps of coastal tidal flats in China at high spatial resolution.

Supervised and unsupervised classification methods (e.g., support vector machine (SVM) classifier) (Arino et al., 2008; Friedl et al., 2010; Friedl et al., 2002; Gong et al., 2013; Hansen et al., 2000; Loveland et al., 2000), and object-based classification (Dronova et al., 2015) have been widely used to produce most of the land cover products. These methods usually produced accurate land cover maps for small regions at a specific time, but were often costly, time consuming, difficult to scale-up to larger areas, and couldn't be used to analyze broader spatio-temporal variability and trends (Chen et al., 2017; Ghosh et al., 2016). Moreover, most of these studies used imagery from a single date or multiple dates to produce wetland maps. Due to the periodicity of tides, phenology of coastal vegetation, and bad-quality observations, the classification of wetlands by using specific imagery or one composite image often have large spatio-temporal uncertainties (Chen et al., 2017). Murray et al. (2014, 2012) used regional tidal models and selected Landsat images (close to high and low tides) to map coastal wetlands. This method assumed that coastal wetlands changes in the intertidal zones are small over the time period taken to acquire satellite images (Mason et al., 2010). However, areas of wetlands in China have changed a lot because of increased economic development (Niu et al., 2012). Chen et al. (2016) visually interpreted high tidal coastline locations and tidal flats in Yangtze Estuary, but this method is insufficient at tracking tidal flats in national scale. Li and Gong (2016) determined the annually inundated area and coastline dynamics of western Florida using time series Landsat images, but tidal flats weren't extracted within the inundated area. Tide-covered lands can be estimated by using tidal gauge records and Digital Elevation Model (DEM) (Zhao et al., 2008), however the tidal record may be incomplete and at a coarse temporal resolution for long temporal ranges (Bell et al., 2016).

Increase in freely available time series remote sensing data has generated intense interest within the geoscience community to investigate land cover change history and increased demand for advanced and efficient hardware and software processing capabilities (Casu et al., 2017; Chen et al., 2017; Dong et al., 2016). In the last few years, cloud-based computing capacity has improved greatly and shows great potential for large-scale land cover mapping. For example, Google Earth Engine (GEE), which consists of a multi-petabyte analysis-ready data with a high-performance cloud computing platform, has enabled researchers to quickly process millions of images in an intrinsically-parallel processing way (Casu et al., 2017; Gorelick et al., 2017). All images archived in GEE could be used to generate global and national land cover maps. Several studies have used GEE to analyze time series spectral data of individual pixels to produce annual maps of paddy rice (Dong et al., 2016; Dong et al., 2015; Zhang et al., 2015a; Zhang et al., 2017), algal blooms (Hu et al., 2010; Zhang et al., 2015b), forests (Chen et al., 2018; Chen et al., 2017), and open surface water bodies (Pekel et al., 2016; Zou et al., 2018; Zou et al., 2017). A recent study also analyzed time series Landsat images during 1987–2015 and continental-scale tidal modelling data, and reported spatial-temporal changes of coastal wetlands (intertidal zone) in Australia (Sagar et al., 2017).

In this study, we aim to study spatio-temporal dynamics of the coastal tidal flats in China from 1986 to 2016 using time series Landsat TM/ETM + /OLI images and GEE cloud computing platform. The specific objectives of this study were to: (1) develop a simple and robust mapping algorithm to generate annual maps of coastal tidal flats, and analyze the inter-annual variations of tidal flats area in China during 1986–2016; (2) analyze spatio-temporal changes (erosion and expansion) of coastal tidal flats in the Yellow River delta and Yangtze River

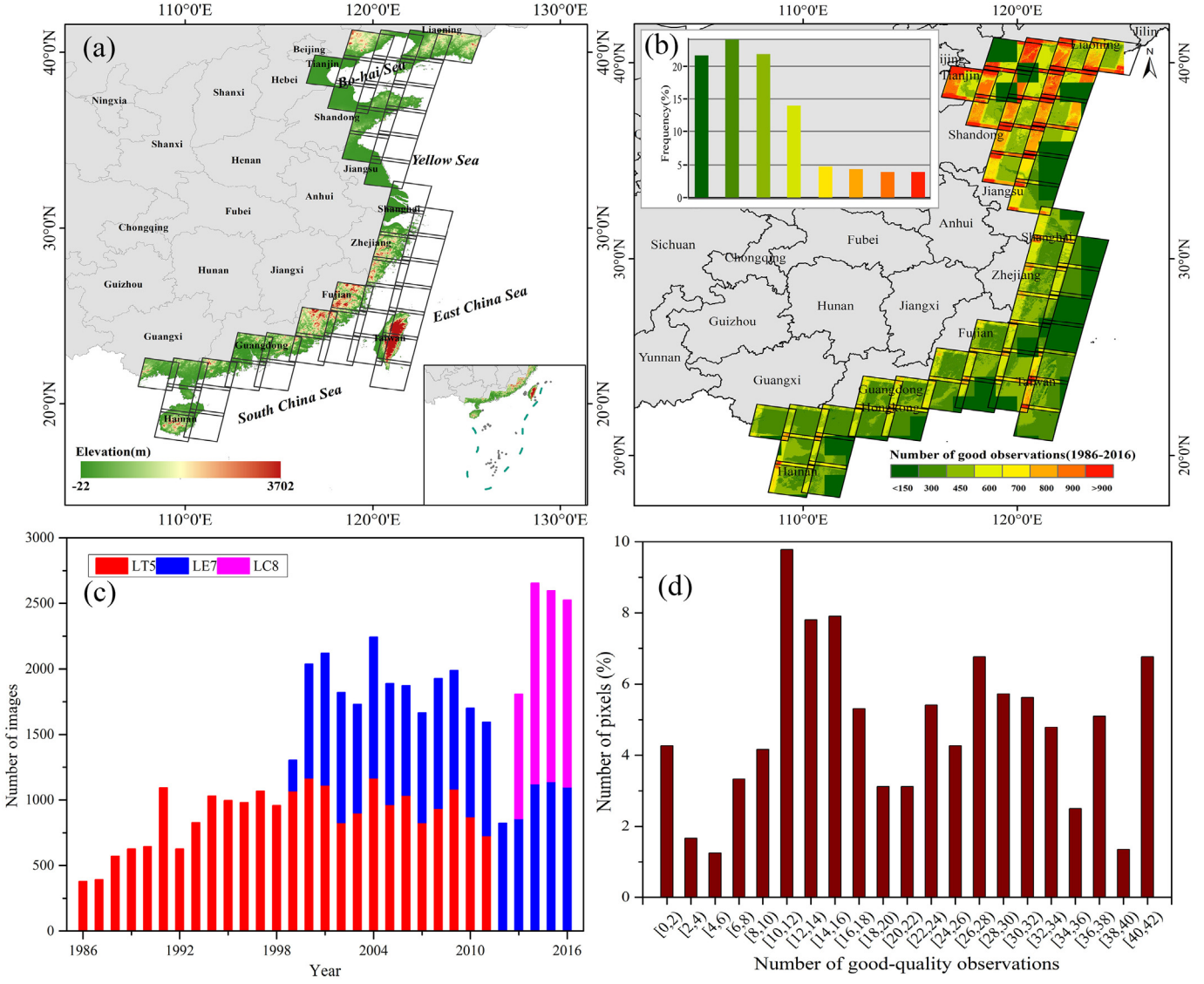

Fig. 2. Location of study area and availability of time series Landsat images from 1986 to 2016. (a) Location of study area and coverage of Landsat Worldwide Reference System 2 (WRS-2) path/row, (b) the number of all Landsat images in each path/row, (c) total numbers of images by sensors (Landsat 5/7/8), and (d) the distribution of good-quality observation numbers of all pixels from 1986 to 2016.

delta during 1986–2016, and (3) identify the major factors that have driven the observed changes in coastal tidal flats.

2. Materials and methods

2.1. Study area

China's coastal zone stretches from the mouth of the Yalu River in the north to the estuary of Beilun River in the south (18.2°N to 40.5°N) and the coastline covers approximately 18,000 km. It includes Hong Kong, Macao, Taiwan and the provinces of Liaoning, Tianjin, Hebei, Shandong, Jiangsu, Shanghai, Zhejiang, Fujian, Guangdong, Guangxi Zhuang Autonomous, and Hainan. It covers three climate zones: tropical, sub-tropical, and temperate climate (Liu et al., 2014). Most of the northern half is low lying, although some of the mountains and hills of Northeast China and the Shandong Peninsula extend to the coast. The elevation of the China's coastal zone ranges from sea level to over 3700-m above sea level (Fig. 2a).

2.2. Landsat data and pre-processing

The study area covers 46 path/row (tiles) of the Landsat Worldwide Reference System (WRS-2) (Fig. 2a). We used all the available standard level 1 Terrain-corrected (L1T) orthorectified Landsat images between January 1, 1986 and December 31, 2016, which have been archived in the GEE platform as the image collection of United States Geological Survey (USGS) Landsat 5/7/8 Surface Reflectance (SR). We counted the number of Landsat images in each path/row (Fig. 2b), total observation numbers of individual pixels by sensors (Landsat5/7/8) (Fig. 2c), and the distribution of good-quality observation numbers of all pixels from 1986 to 2016 (Fig. 2d). The frequencies of the first interval (0–2) and the second interval (2–4) were 4.3% and 1.7%, respectively, and > 94% of the pixels had 4 or more good-quality observations from 1986 to 2016. Bad-quality observations, including clouds, cloud shadows, cirrus, snow/ice and scan-line corrector (SLC)-off gaps, were identified using the Fmask band and not included in data analyses (Zhu et al., 2015; Zhu and Woodcock, 2012). All Landsat image pre-processing tasks were carried out in the GEE platform.

Three widely used vegetation indices (VIs) and one water-related spectral index were calculated from the surface reflectance data with

good-quality observations: Nominalized Difference Vegetation Index (NDVI) (Tucker, 1979), Enhanced Vegetation Index (EVI) (Huete et al., 2002; Huete et al., 1997), Land Surface Water Index (LSWI) (Gao, 1996; Xiao, 2004), and modified Normalized Difference Water Index (mNDWI) (Xu, 2006). NDVI and EVI are related to vegetation greenness, LSWI is sensitive to vegetation water content and soil water, and mNDWI is sensitive to open surface water body. These indices have been used to identify vegetation (Huete et al., 2002; Xiao et al., 2006) and open surface water body (Chen et al., 2017; Xu, 2006; Zou et al., 2018; Zou et al., 2017).

$$NDVI = \frac{\rho_{nir} - \rho_{red}}{\rho_{nir} + \rho_{red}} \quad (1)$$

$$EVI = 2.5 \times \frac{\rho_{nir} - \rho_{red}}{\rho_{nir} + 6 \times \rho_{red} - 7.5 \times \rho_{blue} + 1} \quad (2)$$

$$LSWI = \frac{\rho_{nir} - \rho_{swir}}{\rho_{nir} + \rho_{swir}} \quad (3)$$

$$mNDWI = \frac{\rho_{green} - \rho_{swir}}{\rho_{green} + \rho_{swir}} \quad (4)$$

where ρ_{blue}, ρ_{green}, ρ_{red}, ρ_{nir}, and ρ_{swir} are blue (450–520 nm), green (520–600 nm), red (630–690 nm), near-infrared (NIR: 760–900 nm), and shortwave infrared (SWIR: 1550–1750 nm) bands of Landsat TM/ETM+/OLI imagery, respectively.

2.3. Data on river sediment load, controlled soil and water loss and afforestation

The long-term river sediment load data in the Yangtze River Delta were recorded at the Datong Station and were acquired from the Bulletin of China River Sediment (BCRS) from 1986 to 2011 (available at: www.cjh.com.cn) (Wei et al., 2015). The sediment load data in the Yellow River Delta were acquired at the Lijin Station from 1986 to 2014, the last gauging station approximately 100 km upstream from the river mouth (Pan and Mei, 2017; Wu et al., 2017). Data about controlled soil and water loss area and afforestation areas in each province in China from 1995 to 2016 were collected from the China Statistical Yearbook from National Bureau of Statistics of the People's Republic of China (available at: http://www.stats.gov.cn/tjsj/ndsj). All these data were used to analyze the main driving factors for spatio-temporal dynamics of tidal flats in China's coastal zone.

2.4. Algorithms to identify open surface water body, vegetation and tidal flats in the coastal zone

Coastal wetlands could be divided into two major parts along a gradient from inland to sea: coastal vegetation and tidal flats (Fig. 1). Here we describe our algorithms and workflows to identify and generate annual maps of coastal tidal flats in China from 1986 to 2016.

2.4.1. Algorithms to identify open surface water body

Although mNDWI was widely used to detect water bodies (Davranche et al., 2010; Feng et al., 2012; Feyisa et al., 2014; Xu, 2006), it has commission errors in mixed pixels with water body and other land cover types, especially when the pixel comprises vegetation and water body (Santoro et al., 2015). To reduce the effects of vegetation on identifying water body, we combined the mNDWI and two greenness-based vegetation indices (EVI and NDVI) to detect open surface water body. About 2541 points (pixels), of which 1268 were water and 1273 were non-water during coastal zone of China were selected using visual interpretation and delineation of very high-resolution images (Fig. S1). 99.10% of the water points have mNDWI > EVI while 97.13% of the non-water pixels show mNDWI < EVI (Fig. S2a). Thus, mNDWI > EVI is a good criterion to detect water. Also, 98.99% of the water pixels have mNDWI > NDVI while 97.46% of the non-water pixels show mNDWI < NDVI (Fig. S2b). Therefore, mNDWI > NDVI can be used as a supplementary criterion to separate water from non-water pixels. Furthermore, 99.76% of the water pixels show EVI < 0.1 (Fig. S2c). Thus, EVI < 0.1 can be used to exclude mixed pixels of water and vegetation. The final water detection formula is ((mNDWI > EVI or mNDWI > NDVI) and EVI < 0.1). This mNDWI plus VI algorithm was first implemented in Oklahoma (Zou et al., 2017), then used again using ~12,000 randomly sampled Landsat pixels across the contiguous United States, and showed an overall accuracy of 96.91% with a kappa coefficient of 0.94 (Zou et al., 2018). Furthermore, this algorithm had been compared with other water detection algorithms, including TCW, AWEI, and mNDWI (Zhou et al., 2017). Results showed that this mNDWI plus VI algorithm had high average producer's accuracy (98.1%) and user's accuracy (91.0%) between Landsat 7 ETM+, Landsat 8 OLI, and Sentinel-2 MSI.

2.4.2. Algorithms to identify green vegetation

NDVI is strongly linked to the leaf area index (LAI). However, it could result in saturation where the vegetation canopy is closed and is sensitive to atmospheric conditions and soil background (Huete et al., 2002; Xiao et al., 2003). EVI adjusts the reflectance in the red band as a function of the reflectance in the blue band, and it accounts for residual atmospheric contamination (e.g., aerosols), variable soil conditions, and canopy background reflectance (Huete et al., 2002; Huete et al., 1997). In addition to NDVI and EVI, LSWI has also been used to identify vegetation and exclude water bodies. Therefore, we use (EVI ≥ 0.1, NDVI ≥ 0.2 and LSWI > 0) to identify green vegetation (Xiao et al., 2009).

2.4.3. Annual frequency maps of open surface water body and green vegetation

Due to the periodicity of tidal dynamics, phenology of coastal vegetation, and bad-quality observations, wetland classification results derived from one image or one composite image do not capture such dynamics. To reduce the effects of tidal dynamics and phenology on coastal wetlands mapping, a frequency-based approach from time series Landsat images was used to identify coastal vegetation area and tidal flats (non-vegetated areas) in the intertidal zone, between inland and year-long sea water. Open surface water body is first determined for one observation using Eq. (5), and then, water body frequency in a year is calculated using Eq. (6).

$$Water = \begin{cases} 1 & \text{EVI} < 0.1 \text{ and (mNDWI>EVI or mNDWI>NDVI)} \\ 0 & \text{Other values} \end{cases} \quad (5)$$

$$F_{Water} = \frac{\sum N_{Water}}{\sum N_{Total} - \sum N_{Bad}} \quad (6)$$

where F_{Water} is the frequency of open surface water body scaled to 0 and 1 among all the good-quality observations, ΣN_{Water} is the number of open surface water bodies calculated using Eq. (5), ΣN_{Total} is the total number of observations in a year, ΣN_{Bad} is the number of bad-quality observations in a year, and $\Sigma N_{Total} - \Sigma N_{Bad}$ is the number of good-quality observations. Fmask values represent for different image quality, such as 0 for clear land pixel, 1 for clear water pixel, 2 for cloud shadow, 3 for snow, and 4 for cloud (Zhu et al., 2015; Zhu and Woodcock, 2012). Thus, we identified those pixels with Fmask values > 1 as bad-quality observations and then masked out or excluded them from the study.

Similarly, we used the Eq. (7) and Eq. (8) to calculate the vegetation frequency map.

$$Vegetation = \begin{cases} 1 & \text{EVI} \geq 0.1 \text{ and NDVI} \geq 0.2 \text{ and LSWI} > 0 \\ 0 & \text{Other values} \end{cases} \quad (7)$$

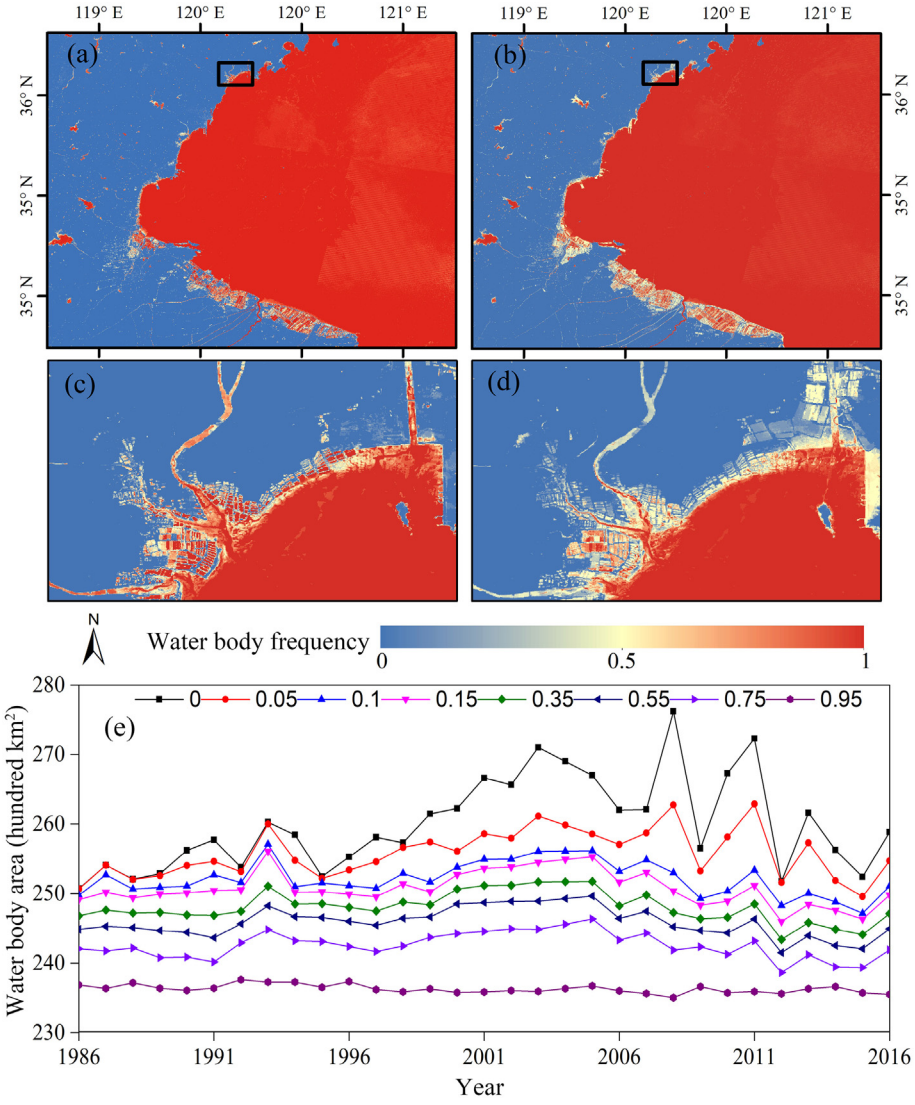

Fig. 3. Frequency maps of surface water body and water body areas using different frequency thresholds: (a) water body frequency map in 2016, (b) 31-year average frequency map of surface water body over 1986–2016, (c) zoom-in show the local details of frequency map in 2016, (d) zoom-in show the local details of average frequency map over 1986–2016, (e) surface water body areas using different frequency thresholds.

$$F_{Vegetation} = \frac{\sum N_{Vegetation}}{\sum N_{Total} - \sum N_{Bad}} \quad (8)$$

2.4.4. Annual maps of coastal tidal flats

In previous studies of inland freshwater bodies, year-long water was identified using 0.75 as the threshold of open surface water body frequency in the open surface water body mapping in Oklahoma (Zou et al., 2017) and the contiguous US (Zou et al., 2018). Note that sea water is less frequently impacted by precipitation, snowmelt and other factors. The frequency maps of open surface water body in representative region in East China Sea in 2016 (Fig. 4a and c) and 31-year frequency map over 1986–2016 (Fig. 3b and d) had similar spatial patters so that we could identify annual year-long seawater and intertidal zone using water frequency map in each year. We generated and calculated annual water body frequency maps and total surface water body areas by different frequency thresholds for individual years (Fig. 3e). The number of pixels (total area) with water body frequency > 0.95 for individual years have small interannual variation during 1986–2016. We also evaluated the spatial distribution of different frequency thresholds (Fig. S3). When threshold values of 0.75, 0.80, 0.85, 0.90, and 0.95 were selected, the seawater extended to the ocean constantly. When the threshold is 0.96, the seawater remained unchanged. Thus, we used 0.95 to define year-long sea water, as well as low water line. We also used 0.05 of water body frequency to identify the highest tidal line because we assumed a potential error range (5%) resulted from the algorithms and image data quality which may be omitted by the Fmask cloud-screening algorithm (Zhu et al., 2015; Zhu and Woodcock, 2012). Therefore, those pixels with a water body frequency spanning from 0.05 to 0.95 were classified as intertidal zone.

We selected six large coastal vegetation areas of interest (AOIs) to study their distributions of vegetation and water frequency (Fig. 4a-f). According to the distribution of vegetation frequency of AOIs (Fig. 4g and h), the threshold value of 0.05 was used as the threshold to classify coastal vegetation area (vegetation frequency ≥ 0.05) and non-vegetated tidal flats (vegetation frequency < 0.05).

Several land cover types, such as ponds, salt pans, and wharfs may affect the accuracy of tidal flat maps as they have similar characteristics: low vegetation frequency and temporary inundation. Fortunately, those features which affected the accuracy of the maps account for a small percentage of all tidal flats so that visual interpretation was used to identify and remove ponds, salt pans, and wharfs to improve map accuracy.

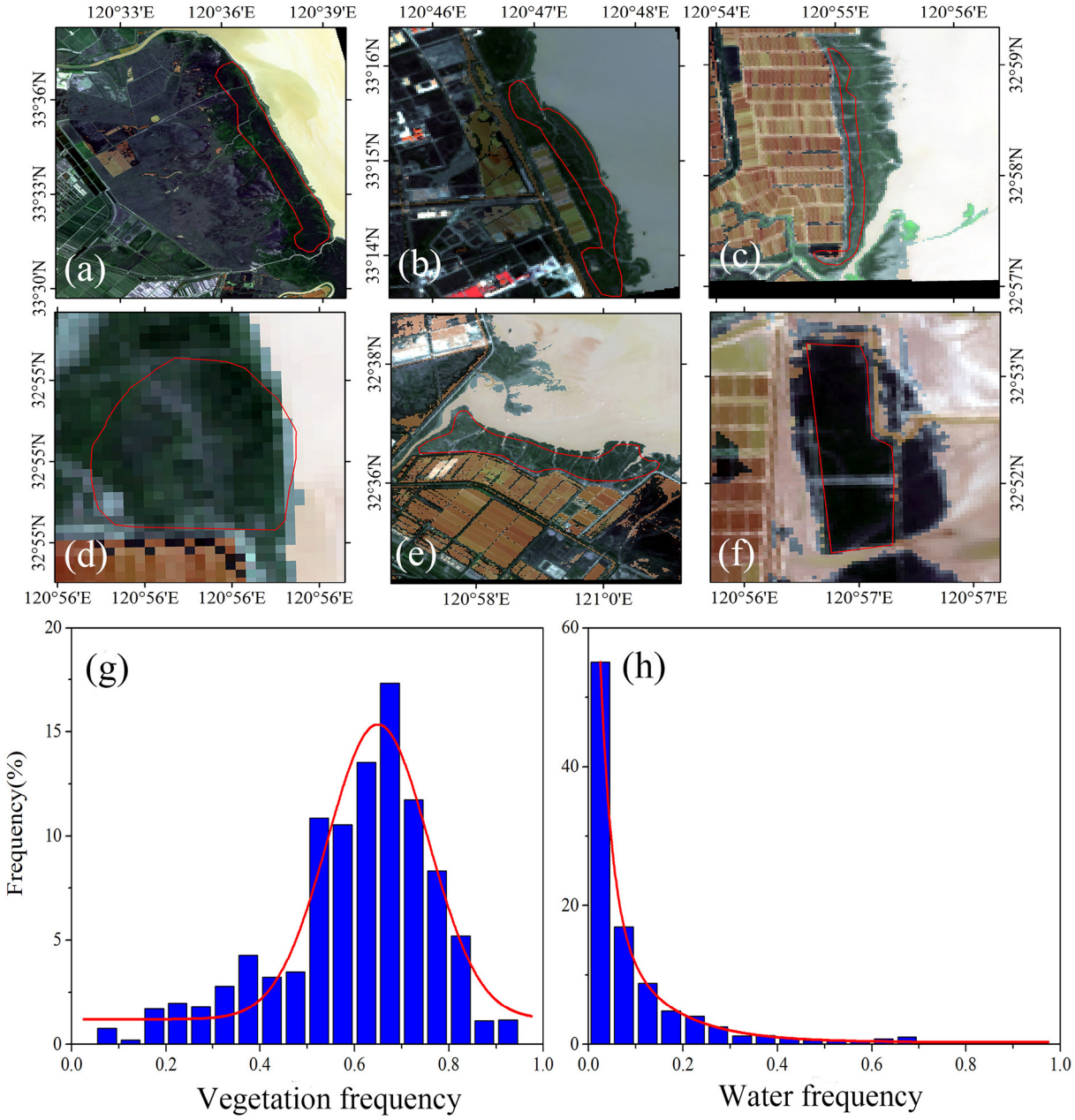

Fig. 4. Location of selected coastal vegetation areas of interest (AOIs) and their pixel distribution of vegetation and water frequency. (a-f) the location of coastal vegetation AOIs, (g) vegetation frequency distribution, (h) water body frequency distribution.

2.5. Accuracy assessment of annual map of tidal flats in 2016 from Landsat images

The annual maps of tidal flats in China were generated using above-mentioned Landsat images, algorithms and GEE platform. We used the stratified random sampling approach and very high resolution (VHR) images from Google Earth to assess the accuracy of tidal flats map in 2016. First, the study area was partitioned into two classes (tidal flats and non-tidal flats which include green vegetation, open surface water body). Second, random points were generated in each stratum using ArcGIS, and then we delineated the AOIs as circle buffers of the points (30-m) (Chen et al., 2017). Third, the AOIs were converted to Keyhole Markup Language (KML) format in ArcGIS and loaded into Google Earth. Each AOI was checked using the VHR images and labeled the pure land cover AOIs. The AOIs without clear land cover information were excluded. Finally, a total of 11,683 AOIs were generated for the validation of two map layers: tidal flats (2162 AOIs) and non–tidal flats (9521 AOIs) (Fig. S4). Then a confusion matrix was calculated to evaluate the accuracy of the results.

2.6. Inter-comparison and spatio-temporal analyses of annual maps of tidal flats

As most existing land cover maps do not delineate coastal tidal flats, and existing researches have classified wetlands only in small regions of China (Chen et al., 2016; Chu et al., 2006; Murray et al., 2014; Yao, 2013), we compared our tidal flat maps with those publications that include tidal flat layer.

To analyze the spatio-temporal variations of tidal flats in China, first we analyzed the distribution of tidal flats in different coastal provinces in 2016. Then, we calculated the total areas of tidal flats in China and different provinces over the past 31 years (1986–2016) using the

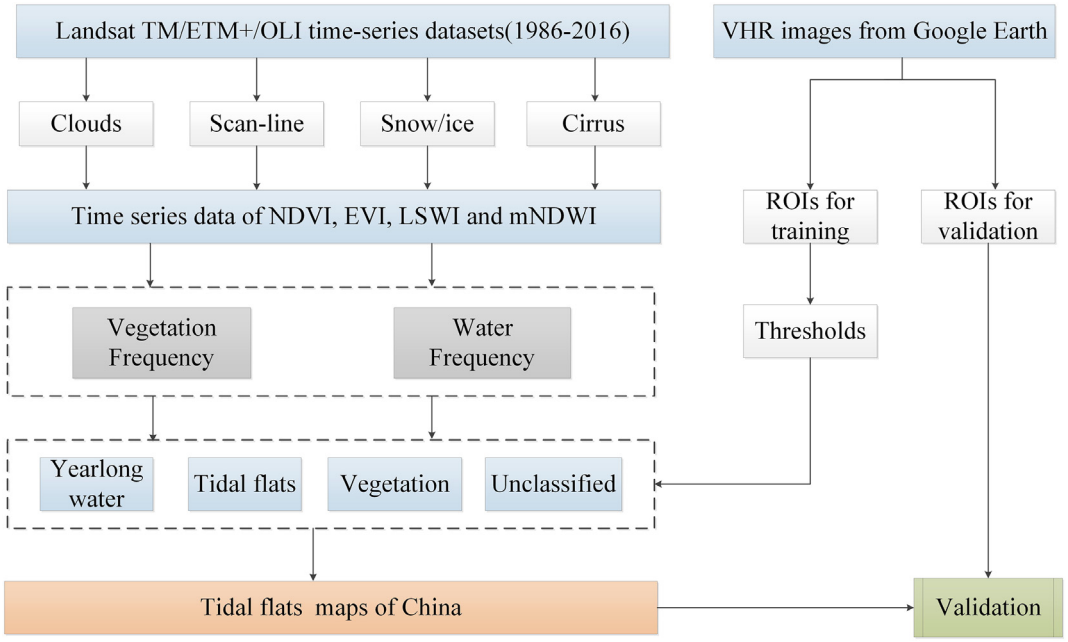

Fig. 5. Workflow of tidal flats mapping using Landsat time-series images from 1986 to 2016.

coordinate of Projected Coordinate System of Krasovsky_1940_Albers and analyzed their inter-annual variations using simple linear regression analysis. Detailed spatio-temporal changes, as well as erosion and expansion trends of tidal flats, were also analyzed in two representative regions: Chongming Island in Yangtze River Delta and Yellow River Delta. Chongming Island is regarded as the largest alluvial island in the estuary of a river and the largest sand island in the world. Yellow River is regarded as the second largest river in the world in terms of sediment discharge (Bi et al., 2014). The workflow for mapping tidal flats (1986–2016) was showed in Fig. 5.

3. Results

3.1. Tidal flats map in 2016 across the coastal zone of China

Fig. 6. shows the spatial distribution of tidal flats along the coastal zone of China in 2016, which is organized into four main parts for easy visualization: Bohai Sea, Yellow Sea, East China Sea, and South China Sea. Three figures that show the local details of tidal flats in selected regions and the administrative region map in 1980s in China were also shown in Fig. 6. The confusion matrix of land cover validation was calculated and the result shows that the tidal flats map in 2016 had high user's accuracy (96.3%), producer's accuracy (91.0%), and overall accuracy (97.6%) with a kappa coefficient of 0.92 (Table 1).

The total area of tidal flats in China in 2016 was about 731,170 ha. The tidal flats in the provinces around Yellow River Delta (Hebei, Tianjin, Shandong) and Pearl River Delta (Fujian, Guangdong, Hong Kong, Macao, and Guangxi provinces) accounted for about 72% of total tidal flats in China in 2016. Shandong had the largest tidal flat area (224,940 ha). Jiangsu and Zhejiang around Yangtze River Delta had relatively larger areas of tidal flats, covering about 46,774 ha and 64,105 ha, respectively. Shanghai had the least tidal flats area as it is the smallest province in China coastal zone. About 20,676 ha and 25,070 ha of tidal flats were found in Liaoning and Taiwan provinces, respectively. Northern China had a larger area of tidal flats than southern China, and tidal flats areas decreased significantly from Fujian to Hainan Province (Table 2).

As the High Water Line (HWL) has been widely used to define the coastline (Ford, 2013; Ghosh et al., 2015; Pardo-Pascual et al., 2012), we digitized the HWL (water frequency = 0.05), calculated the length of coastline and mean tidal flats width using coastline length and tidal flats area within each province in 2016 (Table 2). The total length of China coastline is about 24,609 km. Guangdong (including Hong Kong and Macao) and Liaoning Provinces had smaller mean tidal flats width than other provinces due to their long coastlines. Tianjin Province had largest mean tidal flats width due to its short coastline and high sediment.

3.2. Annual dynamics of tidal flats areas during 1986–2016 at national and provincial scales

The total tidal flats area in China had large interannual variation from 1986 through 2016 (Fig. 7). The annual tidal flats area varied from 8.54×10^5 ha in 1986, 1.20×10^6 ha in 2001 to 7.31×10^5 ha in 2016, with an average area of 9.47×10^5 ha. It clearly has (1) a stable period (1986–1992, $R^2 = 0.02$), (2) an increasing period (1993–2001, $R^2 = 0.89$, $p < 0.01$), and (3) a decreasing period (2002–2016, $R^2 = 0.96$, $p < 0.01$) in the last 31 years.

Different provinces showed different trends over the three decades. Coastal tidal flats areas in Hebei, Tianjin, Shandong, Jiangsu, and Shanghai showed similar trend with the total tidal flats area in China during 1986 and 2016. However, significant decreasing trends were founded in the provinces of Liaoning ($R^2 = 0.95$, $p < 0.01$) and Guangdong (including Hong Kong and Macao) ($R^2 = 0.82$, $p < 0.01$). Zhejiang, Fujian, and Hainan showed slight decreasing trend. Guangxi and Taiwan had little variation during 1986 and 2016.

3.3. Erosion and expansion of coastal tidal flats in Yellow River and Yangtze River Deltas

Coastal tidal flats of China are too long from north to south to be showed in a full map, and tidal flats in various places showed different erosion and expansion patterns and dynamics. To identify the erosion and expansion trend of tidal flats, we selected two case-study regions: (1) Chongming in Yangtze River Delta and (2) Yellow River Delta (Fig. 8a and d). Tidal flats maps in 1986, 1991, 1996, 2001, 2006, 2011, and 2016 (Fig. 8b and e), as well as the annual area trend during 1986–2016 (Fig. 8c and f), were shown in Fig. 8.

Tidal flats areas in Chongming showed a statistically significant decreasing trend (1986–1991, $R^2 = 0.94$, $p < 0.01$) and increasing

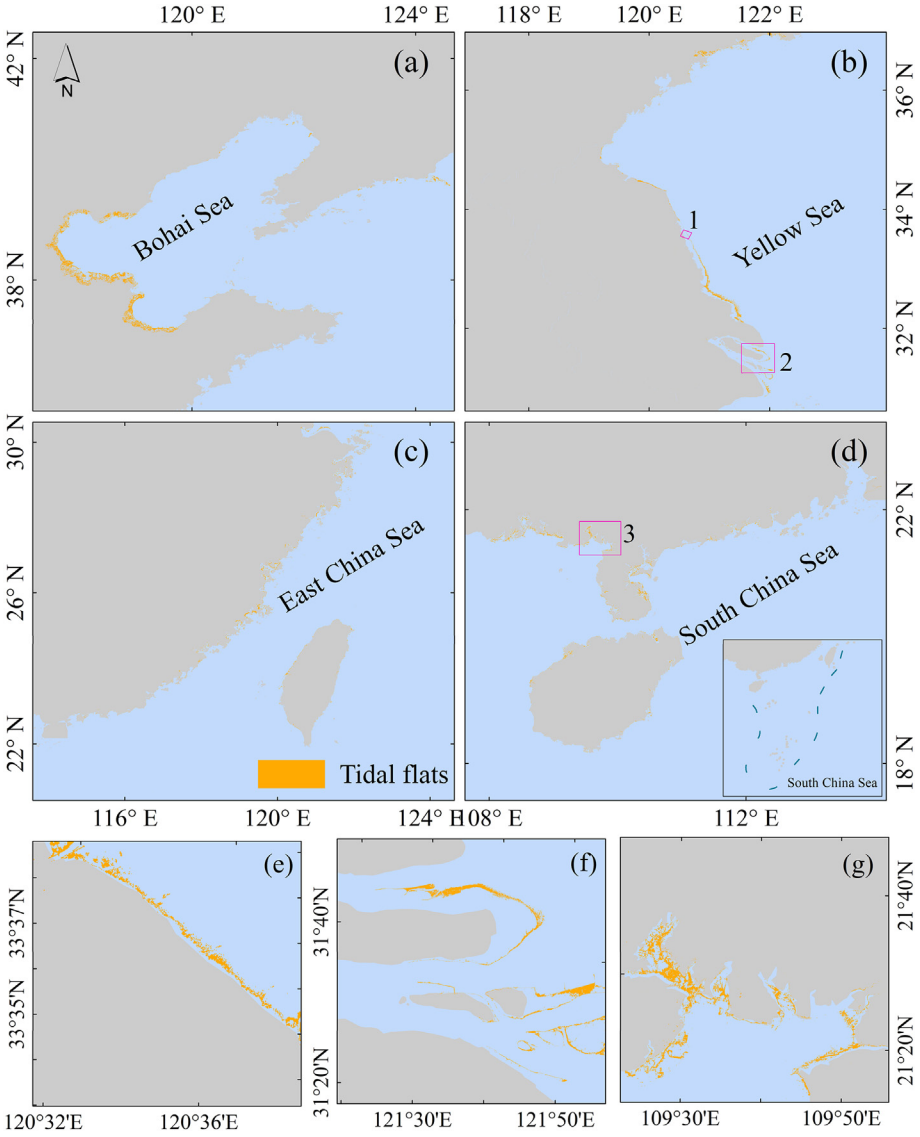

Fig. 6. The administrative region map in 1980s and four parts of the resulting tidal flats map in China in 2016: (a) Bohai Sea, (b) Yellow Sea, (c) East China Sea, and (d) South China Sea, and (e, f, g) are three zoom-in views for the case regions labeled as 1,2,3, respectively.

trend (1992–2016, $R^2 = 0.32$, $p < 0.01$) over the last 31 years. The area decreased from 8581 ha in 1986 to 3589 ha in 1991, then increased significantly to 10,995 ha in 2016 (Fig. 8c). The tidal flats in Chongming had clearly expanded into the ocean over the past 31 years (Fig. 8b).

As for the Yellow River Delta (YRD), engineers blocked the main channel and forced the river to veer northeast in 1996, which caused sediment to be deposited in a new location. The spatial distribution of tidal flats on our maps reflected the outcomes of this project clearly (Fig. 8e). The annual tidal flats area was highly variable from 1986 to 2016 and increased from 50,497 ha in 1986 to 81,301 ha in 1998, and then decreased to 48,254 ha in 2016.

To identify the speed of erosion and expansion in these two deltas, we randomly selected a base-point and two representative reference lines: L-east which across the mouth of the rivers and L-north which was perpendicular to L-east (Fig. 9a and c). The trends of erosion and expansion were calculated using the distance from the outside edge of tidal flats to the base-point in different years. Tidal flats in Chongming showed expansion with different rates in different orientations. The expansion rate of L-east decreased from 1.7 km/5 years during 1986–1991 to 0.6 km/5 years during 2011–2016. However, the expansion rate of L-north was relatively stable with an average rate of

Table 1
Confusion matrix of tidal flats validation based on the areas of interest (AOIs) from very high-resolution images of Google Earth.

		Ground reference pixels		Total map pixels	User's accuracy
	Class	Tidal flats	Non-tidal flats		
Map pixel	Tidal flats	2082	80	2162	96.3%
	Non-tidal flats	205	9316	9521	97.9%
Total ground truth pixels		2287	9396	11,683	OA = 97.6%
Producer's accuracy		91.0%	99.2%		Kappa = 0.92

Table 2
Distribution of tidal flats in different provinces in China in 2016.

Province	Tidal flats area (ha)	Percentage (%)	Coastline length (10^3 m)	Mean tidal flats width (m) (Tidal flats area/coastline length)
Liaoning	20,676	2.8	2494	82.9
Hebei	72,787	10.0	501	1452.8
Tianjin	62,708	8.6	116	5405.9
Shandong	224,940	30.8	896.2	858
Jiangsu	46,774	6.4	704	664.4
Shanghai	10,995	1.5	615	178.8
Zhejiang	64,105	8.7	3427	187.1
Fujian	91,200	12.5	4185	217.9
Taiwan	25,070	3.4	1516	165.4
Guangdong(including Hong Kong and Macao)	55,492	7.6	6034	92.0
Guangxi	22,265	3.0	1038	214.5
Hainan	34,150	4.7	1439	237.3
Total	731,170	100	24,609	297.1

0.53 km/5 years (Fig. 9b).

Tidal flats in Yellow River Delta had different dynamics. The positive and negative values illustrate the expansion and erosion of tidal flats in Fig. 9d, respectively. Tidal flats in L-north showed tidal flats erosion from 1986 to 2016 at a relatively stable rate of 0.58 km/5 years. However, tidal flats in L-east, across the mouth of YRD, expanded at a rate of 7.8 km/5 years from 1986 to 1996. Afterward, the mouth of YRD eroded inland and the erosion rate decreased over years, approximately 4.53 (1996–2001), 2.23 (2001–2006), 1.81 (2006–2011), 1.40 (2011–2016) km/5 years.

4. Discussion

4.1. Reliability and uncertainty of tidal flats mapping using Landsat data and GEE

In this study we demonstrated the feasibility and reliability of developing annual maps of tidal flats at 30-m spatial resolution in China's coastal zone using the Landsat TM/ETM+/OLI images and the GEE cloud computing platform. Thanks to the open access Landsat data, GEE cloud computing platform, simple and robust algorithms, we conducted this study successfully with high classification accuracy (UA/PA/OA > 90%).

Other researchers had completed the wetland classification of the Yellow River Delta using the visual interpretation method and Landsat imageries in 1986, 1991, 1996, 2001, 2006, 2011, and 2016 (Pan and Mei, 2017). The comparison of total tidal flats areas between this study and Pan's publication in the same study region showed that both data products were consistent in 1986, 1991, 1996, and 2011, but the areas in this study were substantially larger than Pan's results in 2001, 2006, and 2016 (Table 3). One of the reasons for the difference is that they selected Landsat images in the above-mentioned years randomly, which could not avoid the effects caused by the periodicity of tidal dynamics, phenology of coastal vegetation and bad-quality observations. We used all the available images within the study period so that more tidal flats could be identified, and the effects of tidal dynamics were reduced in this study. These two tidal flats products also showed good spatial consistency of tidal flats dynamics in the Yellow River Delta, characterized by erosion in the north and expansion in the mouth of the river. Chen et al. (2016) completed wetland classification using water frequency maps and visual interpretation in the Yangtze Estuary. We compared the area of tidal flats in 1990, 1995, 2000, 2005, 2010, and 2014 in Shanghai (Fig. 10a) and Jiangsu (Fig. 10b). The comparison showed similar trends in the two regions and differences of tidal flats areas in Shanghai was larger than in Jiangsu. The differences are mainly because of the detection of high tide coastline location, which was visually interpreted from single cloud free images for each period to produce tidal flats region.

Image data and algorithms are two of the several factors that could affect the accuracy of tidal flats mapping. The quality and the inconsistent availability of input images at temporal and spatial scales has posed significant challenges to land cover mapping (Gong et al., 2013; Hansen et al., 2000). In this study, Landsat data analysis at the pixel level showed that the annual good-quality observations of pixels had

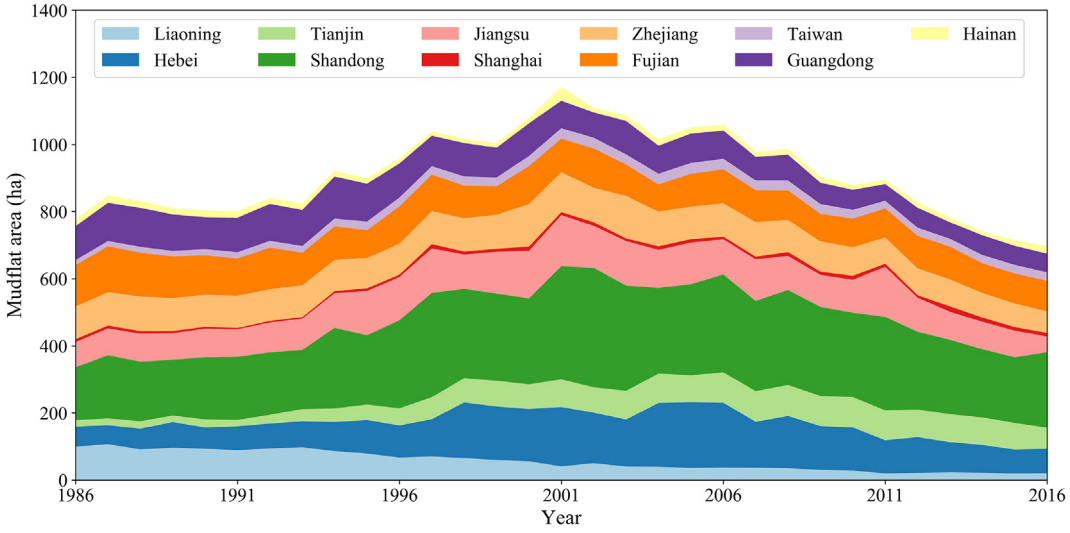

Fig. 7. Inter-annual variations of tidal flats area in different coastal provinces in China from 1986 to 2016.

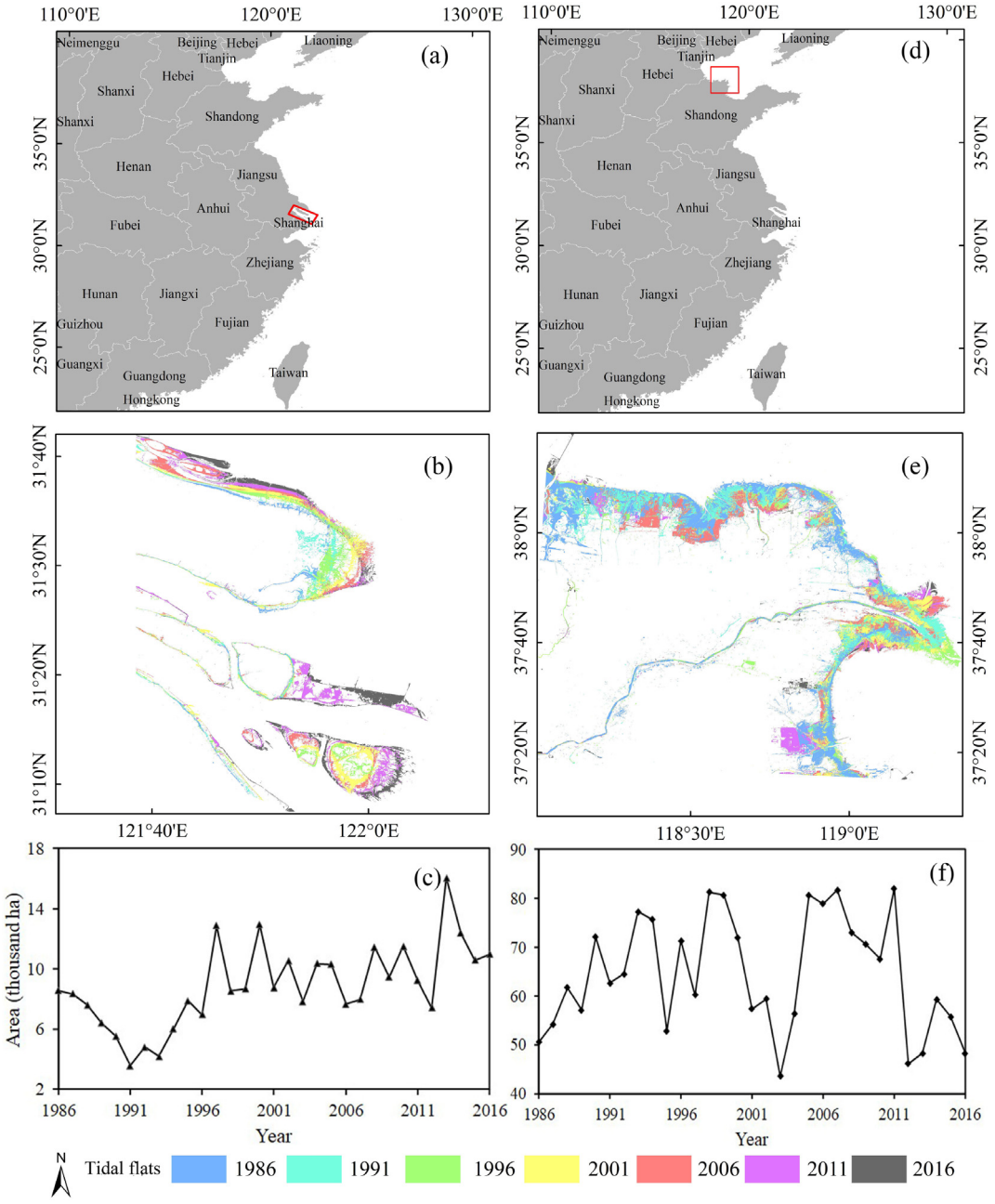

Fig. 8. Location, distribution, and area changes of tidal flats in Chongming in Yangtze River Delta and Yellow River Delta (YRD) during 1986–2016. (a) Location of Chongming, (b) distribution of tidal flats in Chongming, (c) area changes of tidal flats in Chongming, (d) location of YRD, (e) distribution of tidal flats in YRD and (f) area changes of tidal flats in YRD.

notable spatial and inter-annual variations and about 50% of the pixels had less than 15 good-quality observations in a year (Fig. 2). The inconsistent availability of Landsat images could cause some uncertainties in the annual tidal flats maps. Accuracy assessments of annual tidal flat maps had some uncertainties resulting from the limited ground reference data, difficulties in field survey and the limited availability of VHR images over time in Google Earth. To reduce such uncertainties, we produced as many random points as possible to assess the tidal flats map in 2016.

Utilizing a sun-synchronous satellite such as Landsat, it is inevitable that the sensor will only observe a portion of the full tidal range at any location, with less frequent observations at the extremely low and high tides (Dhanjal-Adams et al., 2016; Sagar et al., 2017). Considering the tidal stage changes quickly every month and the number of good-quality observations per year may be limited, year-to-year comparison may not be that accurate, but it is still useful to track the interannual change of tidal flats. There are also significant tidal variations within scene which may affect the tidal flats mapping. In addition, mNDWI plus VI and frequency method were used to detect pure water and pure vegetation in this study so that mixed pixels, such as remnant tidal flats water, couldn't be detected.

4.2. Driving factors for spatio-temporal dynamics of tidal flats in the coastal zone

Several natural and anthropogenic factors have had large influences on tidal flats distribution and dynamics in the coastal zone (Blum and Roberts, 2009; Ma et al., 2014; Morris et al., 2002; Rodriguez et al., 2017). Sediment loads were identified as the major driving factors that influence tidal flats in China (Bi et al., 2014; Chen et al., 2016). Here we

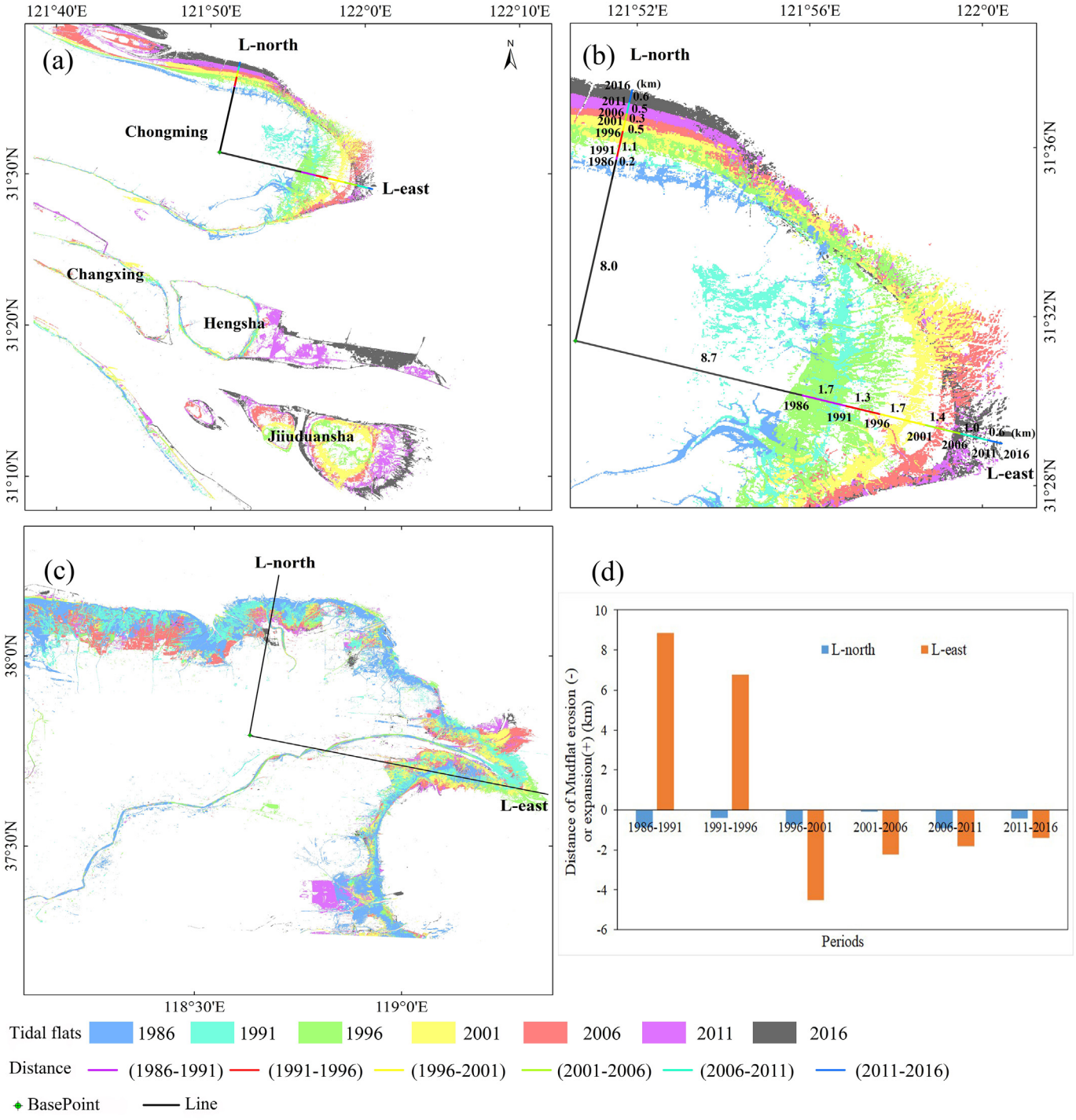

Fig. 9. Measurement of tidal flats erosion and expansion in Chongming in Yangtze River Delta and Yellow River Delta, (a) distribution of tidal flats and reference lines in Chongming, (b) tidal flats changes in Chongming, (c) distribution of tidal flats and reference lines in Yellow River Delta, and (d) tidal flats changes in Yellow River Delta.

Table 3
Comparison with Pan's research (Pan and Mei, 2017) in Yellow River Delta.

	1986	1991	1996	2001	2006	2011	2016
Tidal flats$_{Pan}$	58,814.07	63,655.63	74,313.73	31,996.8	52,776.45	44,288.81	28,385.26
Tidal flats$_{Freq}$	50,497.19	62,643.94	71,364.14	57,349.65	78,868.62	42,009.45	48,257.19

Tidal flats$_{Pan}$: Tidal flats area (ha) from Pan's research using visual interpretation method;
Tidal flats$_{Freq}$: Tidal flats area (ha) in this study using frequency-based method.

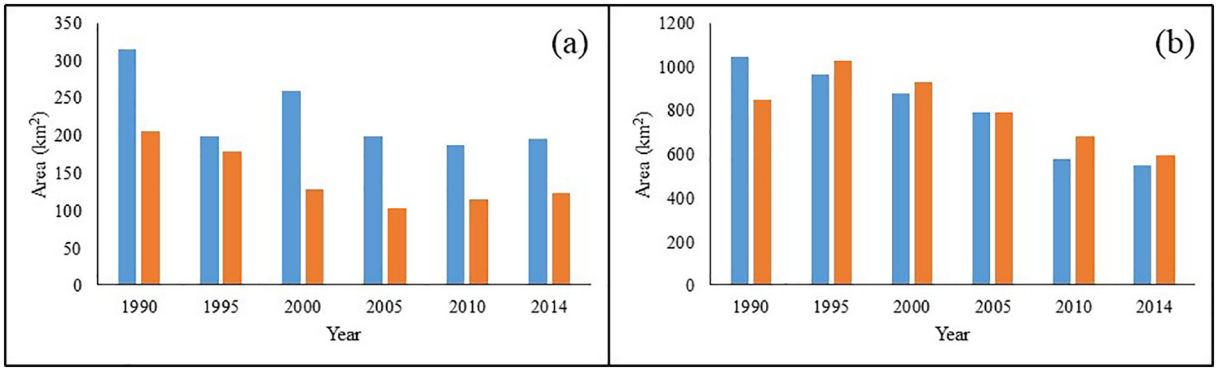

Fig. 10. Area comparison of tidal flats in (a) Shanghai and (b) Jiangsu with Chen's research (Chen et al., 2016).

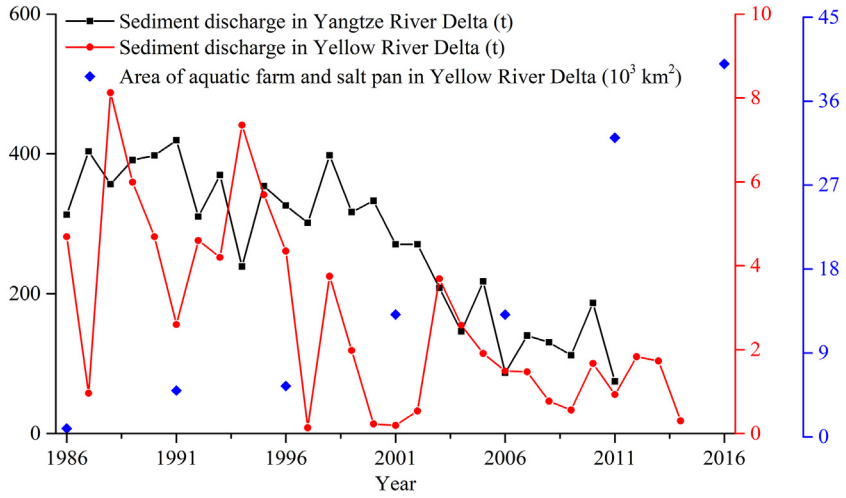

Fig. 11. Inter-annual variations of the area of Aquatic farm and salt pan area, and accumulated sediment discharge in Yellow River Delta and Yangtze River Delta from 1986 to 2016.

collected the sediment loads data from the Datong Station (Wei et al., 2015) in the Yangtze River Delta and the Lijin Station (Pan and Mei, 2017) in the Yellow River Delta to analyze their influences on the area change of tidal flats in China. At the Datong Station, sediment load was high with a large interannual variation during 1986–2000 but had declined linearly since 2001. At the Lijin Station, sediment load was also high during 1986–2003 but started to decline linearly in 2004 (Fig. 11). Another study showed that the sediment discharge to the sea in the Yellow River Delta declined sharply from 0.84 Gt/years to 0.4 Gt/years and 0.15 Gt/year during the periods of 1986–1999 and 2000–2005, respectively (Wang et al., 2007). Reduced sediment load in several stations were also reported in other publications along the Yellow River (Wang et al., 2016) and Yangtze River (Zhao et al., 2017). Tidal flats area dynamics in the coastal zone were affected by both sediment load from rivers (expansion) and erosion to the oceans (loss). High sediment load before the early 2000s could contribute to expansion or stabilization of tidal flats, while reduced sediment load in the 2000s could result in loss of tidal flats areas in the 2000s (Fig. 7), as no sufficient sediment load is available to counter against the tidal flats erosion to the oceans.

Sediment loads are closely associated with the control and conservation of water and soil in China (Zhao et al., 2017). Data about controlled soil and water loss area in China (Fig. S5a) and afforestation areas in each province from 1995 to 2016 (Fig. S5b) were collected from the China Statistical Yearbook. Vegetation cover in China has significantly increased and annual reforestation and afforestation areas in China had remarkable interannual dynamics (Li et al., 2018; Zhang et al., 2018), driven by national policies and ecological engineering and restoration projects. For example, the 'Grain-for-Green' program (GFGP) launched in 1999 resulted in a gradual increase of vegetation during 1995–2001 (Wang et al., 2016), with a large jump in 2002–2003, followed by a decrease in 2004–2006 (Fig. S5a). The area of controlled soil and water erosion has risen steadily since 1995. Most reforestation and afforestation areas were in the two most important basins: The Yellow River Basin and the Yangtze River Basin. Specifically, those provinces in the Yellow River basin had larger afforestation areas than did other regions (Fig. S5b). Accordingly, the changes in total tidal flats area in China were mainly driven by sediment load in the main rivers. Improved soil and water conservation, and increased reforestation and afforestation in China could have contributed to the reduction of tidal flats areas after 2001.

Human activities also played a significant role in driving the change in area, erosion, and expansion of tidal flats in China. For Chongming in the Yangtze River Delta, as an example, anthropogenic land reclamation played a crucial role in the annual area change of tidal flats. Land reclamation in Chongming started on a small scale during 1986 and 1990 and the area of tidal flats decreased at a small rate. After that, three land reclamation projects on a larger scale during 1990–1991, 1992–1992, and 1997–1998 were implemented (Gao and Zhao, 2006), during which tidal flats area declined rapidly. In 2012, the comprehensive control project for *Spartina alterniflora*, which was the major invasive species, was carried out in Chongming Island. A large area of *Spartina alterniflora* was cut, which resulted in bare lands that were identified as tidal flats, causing the tidal flats area increase sharply during 2012–2013. Then, reeds were planted on the bare lands after 2013, which reduced the tidal flats area in 2014–2016 (Fig. 9c).

Similarly, tidal flats in the Yellow River Delta showed large inter-annual variations from 1986 through 2016 (Fig. 8f) due to its large area and human activities. For example, tidal flats were converted into aquatic farms and salt pans for economic benefits (Fig. 11 and Fig. S6) (Pan and Mei, 2017). In addition, policies and ecological projects also affected tidal flats area. An ecological water diversion project for the Yellow River Delta Nature Reserve was carried out in 2011 and approximately 3.5×10^7 m^3 water were transferred into the Yellow River Delta (Zheng et al., 2012). Tidal flats became inundated, which resulted in a sharp decreasing of tidal flats area during 2011–2012 (Fig. 8f).

4.3. Implications for applications and future development

Tidal flats in the coastal zone could serve as the base for offshore fisheries and provide habitats for many aquatic and migratory organisms that contribute to the health of marine ecosystems (Ma et al., 2014). The resulting annual maps of tidal flats in China from 1986 to 2016 at 30-m spatial resolution in this study are useful for better understanding of the interaction between waterfowl populations and change of tidal flats area in the East Asian-Australasian flyway (Rodriguez et al., 2017), which currently is the migratory path for the highest proportion (19%) of threatened waterbird populations among the global flyways (Ma et al., 2014; Ma et al., 2013; Wilson et al., 2011). Also, annual tidal flats maps in this study serve as the dataset for studying the interaction between the tidal flats and tides, sea level rise, and ecological engineering projects under the context of climate change.

The frequency-based land cover mapping algorithms, time series Landsat images, and GEE cloud computing platform, when used together, can maximize the use of available imageries and have the potential to be applied widely (1) to map saltmarsh or mangrove using the annual frequency maps of open surface water body and coastal vegetation, and (2) to monitor the change of coastline and wetlands as they are always affected by the tidal dynamics. Currently, this work was limited by the quality and quantity of Landsat images. A number of multi-spectral data with higher spatial and temporal resolutions, such as Sentinel-2 (Belgiu and Csillik, 2018; Pahlevan et al., 2017; Puliti et al., 2018; Veloso et al., 2017) and Worldview 3 (Asadzadeh and de Souza Filho, 2016), are potential data sources for land use and land cover mapping with higher precision. Radar sensors, such as synthetic aperture radar (SAR), can be used for an areal surveillance that is independent of day time and cloud coverage (Gade et al., 2008). Many studies (reviewed by Lewis (1998)) have successfully used SAR images to map surface water bodies and wetlands. For example, SAR data acquired from Shuttle Imaging radar (SIR)-B mission were used to monitor water level (Alsdorf et al., 2000). Bell et al. (2016) used SAR images which acquired by JERS-1to map the morphology of intertidal area. In addition, Sentinel-1 carries a C-band synthetic aperture radar instrument with a 12-day repeat cycle at the equator and 10-m spatial resolution, and has already been used to monitor open surface water body (Chen et al., 2017) and vegetation (Reiche et al., 2018; Veloso et al., 2017). Thus, we could generate annual maps of tidal flats with higher accuracy in the future by improving the mapping algorithms and using more image data (e.g. Landsat, Sentinel-1 and 2, Worldview 3).

5. Conclusions

Previous land cover classifications generally treated the coastal wetland as single land cover type. Our data and knowledge of the spatio-temporal dynamics of coastal tidal flats at large scales have been very limited. Open-access time series Landsat data and the GEE cloud computing platform enable researchers to track the annual changes of coastal tidal flats in China since the 1980s at 30-m spatial resolution. In this study, all Landsat 5/7/8 images from 1986 to 2016 and a pixel and frequency-based approach were used to generate annual 30-m tidal flats maps in China coastal zone over the last 31 years. The Landsat-based time series vegetation indices and water-related spectral index captured the year-long water body, coastal vegetation, and tidal flats with a small number of training datasets and achieved high accuracy. Our approach reduced the effects of tidal dynamics which introduced large uncertainty in previous efforts with a single or composite image. The quality and the inconsistent availability of Landsat images at temporal and spatial scales, along with our algorithms, could have introduced some uncertainty in our tidal flat maps. Other sensors (e.g., Sentinel-1 and 2, Worldview 3) with higher spatial and temporal resolution are becoming available, which will further help improve coastal wetland mapping in the future. Our annual maps of tidal flats in China are likely to provide vital information for geographical, ecological, and public health applications.

Acknowledgements

This study was supported by the National Key Research and Development Program of China (2017YFC1200100), the Natural Science Foundation of China (41601181, 41630528), Key Research Program of Frontier Sciences (QYZDB-SSW-DQC005), Strategic Priority Research Program (XDA19040301) of Chinese Academy of Sciences (CAS), China, and the National Institutes of Health (1R01AI101028-02A1). We thank the Guest Editors of the Time Series Special Issue, Drs. Tom Loveland, Curtis Woodcock, and Martin Herold, as well as three reviewers for their insightful comments and suggestions.

Appendix A. Supplementary data

Supplementary data to this article can be found online at https://doi.org/10.1016/j.rse.2018.11.030.

References

Alsdorf, D.E., Melack, J.M., Dunne, T., Mertes, L.A.K., Hess, L.L., Smith, L.C., 2000. Interferometric radar measurements of water level changes on the Amazon flood plain. Nature 404 (174). https://doi.org/10.1038/35004560.

Arino, O., Bicheron, P., Achard, F., Latham, J., Witt, R., Weber, J.L., 2008. GLOBCOVER the most detailed portrait of Earth. Esa Bull. Sp. Agency. 136, 25–31.

Asadzadeh, S., de Souza Filho, C.R., 2016. Investigating the capability of WorldView-3 superspectral data for direct hydrocarbon detection. Remote Sens. Environ. 173, 162–173. https://doi.org/10.1016/j.rse.2015.11.030.

Barbier, E.B., Koch, E.W., Silliman, B.R., Hacker, S.D., Wolanski, E., Primavera, J., Granek, E.F., Polasky, S., Aswani, S., Cramer, L.A., Stoms, D.M., Kennedy, C.J., Bael, D., Kappel, C.V., Perillo, G.M.E., Reed, D.J., 2008. Coastal ecosystem-based management with nonlinear ecological functions and values. Science 319, 321–323. https://doi.org/10.1126/science.1150349.

Bartholome, E., Belward, A.S., 2005. GLC2000: a new approach to global land cover mapping from Earth observation data. Int. J. Remote Sens. 26, 1959–1977. https://doi.org/10.1080/01431160412331291297.

Belgiu, M., Csillik, O., 2018. Sentinel-2 cropland mapping using pixel-based and object-based time-weighted dynamic time warping analysis. Remote Sens. Environ. 204, 509–523. https://doi.org/10.1016/j.rse.2017.10.005.

Bell, P.S., Bird, C.O., Plater, A.J., 2016. A temporal waterline approach to mapping intertidal areas using X-band marine radar. Coast. Eng. 107, 84–101. https://doi.org/10.1016/j.coastaleng.2015.09.009.

Bi, N.H., Wang, H.J., Yang, Z.H., 2014. Recent changes in the erosion-accretion patterns of the active Huanghe (Yellow River) delta lobe caused by human activities. Cont. Shelf Res. 90, 70–78. https://doi.org/10.1016/j.csr.2014.02.014.

Blum, M.D., Roberts, H.H., 2009. Drowning of the Mississippi Delta due to insufficient sediment supply and global sea-level rise. Nat. Geosci. 2, 488–491. https://doi.org/10.1038/ngeo553.

Casu, F., Manunta, M., Agram, P.S., Crippen, R.E., 2017. Big Remotely Sensed Data: tools, applications and experiences. Remote Sens. Environ. 202, 1–2. https://doi.org/10.1016/j.rse.2017.09.013.

Chen, Y., Dong, J.W., Xiao, X.M., Zhang, M., Tian, B., Zhou, Y.X., Li, B., Ma, Z.J., 2016. Land claim and loss of tidal flats in the Yangtze Estuary. Sci. Rep. 6 (24018). https://doi.org/10.1038/srep24018.

Chen, B.Q., Xiao, X.M., Li, X.P., Pan, L.H., Doughty, R., Ma, J., Dong, J.W., Qin, Y.W., Zhao, B., Wu, Z.X., Sun, R., Lan, G.Y., Xie, G.S., Clinton, N., Giri, C., 2017. A mangrove forest map of China in 2015: analysis of time series Landsat 7/8 and Sentinel-1A imagery in Google Earth Engine cloud computing platform. ISPRS J. Photogramm. Remote Sens. 131, 104–120. https://doi.org/10.1016/j.isprsjprs.2017.07.011.

Chen, B., Xiao, X., Ye, H., Ma, J., Doughty, R., Li, X., Zhao, B., Wu, Z., Sun, R., Dong, J., Qin, Y., Xie, G., 2018. Mapping forest and their spatial-temporal changes from 2007 to 2015 in tropical hainan island by integrating ALOS/ALOS-2 L-Band SAR and

landsat optical images. Ieee J. Sel. Top. Appl. Earth Obs. Remote Sens. 11, 852–867. https://doi.org/10.1109/jstars.2018.2795595.
Chu, Z.X., Sun, X.G., Zhai, S.K., Xu, K.H., 2006. Changing pattern of accretion/erosion of the modem Yellow River (Huanghe) subaerial delta, China: based on remote sensing images. Mar. Geol. 227, 13–30. https://doi.org/10.1016/j.margeo.2005.11.013.
Davranche, A., Lefebvre, G., Poulin, B., 2010. Wetland monitoring using classification trees and SPOT-5 seasonal time series. Remote Sens. Environ. 114, 552–562. https://doi.org/10.1016/j.rse.2009.10.009.
Dhanjal-Adams, K.L., Hanson, J.O., Murray, N.J., Phinn, S.R., Wingate, V.R., Mustin, K., Lee, J.R., Allan, J.R., Cappadonna, J.L., Studds, C.E., Clemens, R.S., Roelfsema, C.M., Fuller, R.A., 2016. The distribution and protection of intertidal habitats in Australia. Emu 116 (208). https://doi.org/10.1071/MU15046.
Dong, J., Xiao, X., Kou, W., Qin, Y., Zhang, G., Li, L., Jin, C., Zhou, Y., Wang, J., Biradar, C., Liu, J., Moore III, B., 2015. Tracking the dynamics of paddy rice planting area in 1986–2010 through time series Landsat images and phenology-based algorithms. Remote Sens. Environ. 160, 99–113. https://doi.org/10.1016/j.rse.2015.01.004.
Dong, J., Xiao, X., Menarguez, M.A., Zhang, G., Qin, Y., Thau, D., Biradar, C., Moore, B., 2016. Mapping paddy rice planting area in northeastern Asia with Landsat 8 images, phenology-based algorithm and Google Earth Engine. Remote Sens. Environ. 185, 142–154. https://doi.org/10.1016/j.rse.2016.02.016.
Dronova, I., Gong, P., Wang, L., Zhong, L.H., 2015. Mapping dynamic cover types in a large seasonally flooded wetland using extended principal component analysis and object-based classification. Remote Sens. Environ. 158, 193–206. https://doi.org/10.1016/j.rse.2014.10.027.
Dyer, K.R., Christie, M.C., Wright, E.W., 2000. The classification of intertidal mudflats. Cont. Shelf Res. 20, 1039–1060. https://doi.org/10.1016/S0278-4343(00)00011-X.
Feng, L., Hu, C.M., Chen, X.L., Cai, X.B., Tian, L.Q., Gan, W.X., 2012. Assessment of inundation changes of Poyang Lake using MODIS observations between 2000 and 2010. Remote Sens. Environ. 121, 80–92. https://doi.org/10.1016/j.rse.2012.01.014.
Feyisa, G.L., Meilby, H., Fensholt, R., Proud, S.R., 2014. Automated Water Extraction Index: a new technique for surface water mapping using Landsat imagery. Remote Sens. Environ. 140, 23–35. https://doi.org/10.1016/j.rse.2013.08.029.
Ford, M., 2013. Shoreline changes interpreted from multi-temporal aerial photographs and high resolution satellite images: Wotje Atoll, Marshall Islands. Remote Sens. Environ. 135, 130–140. https://doi.org/10.1016/j.rse.2013.03.027.
Friedl, M.A., McIver, D.K., Hodges, J.C.F., Zhang, X.Y., Muchoney, D., Strahler, A.H., Woodcock, C.E., Gopal, S., Schneider, A., Cooper, A., Baccini, A., Gao, F., Schaaf, C., 2002. Global land cover mapping from MODIS: algorithms and early results. Remote Sens. Environ. 83, 287–302. doi:Pii S0034-4257(02)00078-0. https://doi.org/10.1016/S0034-4257(02)00078-0.
Friedl, M.A., Sulla-Menashe, D., Tan, B., Schneider, A., Ramankutty, N., Sibley, A., Huang, X.M., 2010. MODIS Collection 5 global land cover: algorithm refinements and characterization of new datasets. Remote Sens. Environ. 114, 168–182. https://doi.org/10.1016/j.rse.2009.08.016.
Gade, M., Alpers, W., Melsheimer, C., Tanck, G., 2008. Classification of sediments on exposed tidal flats in the German Bight using mufti-frequency radar data. Remote Sens. Environ. 112, 1603–1613. https://doi.org/10.1016/j.rse.2007.08.015.
Gao, B.C., 1996. NDWI - a normalized difference water index for remote sensing of vegetation liquid water from space. Remote Sens. Environ. 58, 257–266. https://doi.org/10.1016/s0034-4257(96)00067-3.
Gao, Y., Zhao, B., 2006. The effect of reclamation on mud flat development in Chongming Island, Shanghai. Chinese Agric. Sci. Bull. 22, 475–479. https://doi.org/10.3969/j.issn.1000-6850.2006.08.117.
Ghosh, M.K., Kumar, L., Roy, C., 2015. Monitoring the coastline change of Hatiya Island in Bangladesh using remote sensing techniques. ISPRS J. Photogramm. Remote Sens. 101, 137–144. https://doi.org/10.1016/j.isprsjprs.2014.12.009.
Ghosh, S., Mishra, D.R., Gitelson, A.A., 2016. Long-term monitoring of biophysical characteristics of tidal wetlands in the northern Gulf of Mexico - a methodological approach using MODIS. Remote Sens. Environ. 173, 39–58. https://doi.org/10.1016/j.rse.2015.11.015.
Gong, P., Niu, Z.G., Cheng, X.A., Zhao, K.Y., Zhou, D.M., Guo, J.H., Liang, L., Wang, X.F., Li, D.D., Huang, H.B., Wang, Y., Wang, K., Li, W.N., Wang, X.W., Ying, Q., Yang, Z.Z., Ye, Y.F., Li, Z., Zhuang, D.F., Chi, Y.B., Zhou, H.Z., Yan, J., 2010. China's wetland change (1990–2000) determined by remote sensing. Sci. China Earth Sci. 53, 1036–1042. https://doi.org/10.1007/s11430-010-4002-3.
Gong, P., Wang, J., Yu, L., Zhao, Y.C., Zhao, Y.Y., Liang, L., Niu, Z.G., Huang, X.M., Fu, H.H., Liu, S., Li, C.C., Li, X.Y., Fu, W., Liu, C.X., Xu, Y., Wang, X.Y., Cheng, Q., Hu, L.Y., Yao, W.B., Zhang, H., Zhu, P., Zhao, Z.Y., Zhang, H.Y., Zheng, Y.M., Ji, L.Y., Zhang, Y.W., Chen, H., Yan, A., Guo, J.H., Yu, L., Wang, L., Liu, X.J., Shi, T.T., Zhu, M.H., Chen, Y.L., Yang, G.W., Tang, P., Xu, B., Giri, C., Clinton, N., Zhu, Z.L., Chen, J., Chen, J., 2013. Finer resolution observation and monitoring of global land cover: first mapping results with Landsat TM and ETM+ data. Int. J. Remote Sens. 34, 2607–2654. https://doi.org/10.1080/01431161.2012.748992.
Gorelick, N., Hancher, M., Dixon, M., Ilyushchenko, S., Thau, D., Moore, R., 2017. Google Earth Engine: planetary-scale geospatial analysis for everyone. Remote Sens. Environ. 202, 18–27. https://doi.org/10.1016/j.rse.2017.06.031.
Hansen, M.C., Defries, R.S., Townshend, J.R.G., Sohlberg, R., 2000. Global land cover classification at 1km spatial resolution using a classification tree approach. Int. J. Remote Sens. 21, 1331–1364. https://doi.org/10.1080/014311600210209.
Hodoki, Y., Murakami, T., 2006. Effects of tidal flat reclamation on sediment quality and hypoxia in Isahaya Bay. Aquat. Conserv. Mar. Freshwat. Ecosyst. 16, 555–567. https://doi.org/10.1002/aqc.723.
Hu, C.M., Lee, Z.P., Ma, R.H., Yu, K., Li, D.Q., Shang, S.L., 2010. Moderate Resolution Imaging Spectroradiometer (MODIS) observations of cyanobacteria blooms in Taihu Lake, China. J. Geophys. Res. 115 (C4). https://doi.org/10.1029/2009jc005511.
Huete, A.R., Liu, H.Q., Batchily, K., van Leeuwen, W., 1997. A comparison of vegetation indices global set of TM images for EOS-MODIS. Remote Sens. Environ. 59, 440–451. https://doi.org/10.1016/s0034-4257(96)00112-5.
Huete, A., Didan, K., Miura, T., Rodriguez, E.P., Gao, X., Ferreira, L.G., 2002. Overview of the radiometric and biophysical performance of the MODIS vegetation indices. Remote Sens. Environ. 83, 195–213. https://doi.org/10.1016/s0034-4257(02)00096-2.
Jin, H.R., Huang, C.Q., Lang, M.W., Yeo, I.Y., Stehman, S.V., 2017. Monitoring of wetland inundation dynamics in the Delmarva Peninsula using Landsat time-series imagery from 1985 to 2011. Remote Sens. Environ. 190, 26–41. https://doi.org/10.1016/j.rse.2016.12.001.
Kline, J.D., Swallow, S.K., 1998. The demand for local access to coastal recreation in southern New England. Coast. Manag. 26, 177–190. https://doi.org/10.1080/08920759809362351.
Koch, E.W., Barbier, E.B., Silliman, B.R., Reed, D.J., Perillo, G.M.E., Hacker, S.D., Granek, E.F., Primavera, J.H., Muthiga, N., Polasky, S., Halpern, B.S., Kennedy, C.J., Kappel, C.V., Wolanski, E., 2009. Non-linearity in ecosystem services: temporal and spatial variability in coastal protection. Front. Ecol. Environ. 7, 29–37. https://doi.org/10.1890/080126.
Kolker, A.S., Allison, M.A., Hameed, S., 2011. An evaluation of subsidence rates and sea-level variability in the northern Gulf of Mexico. Geophys. Res. Lett. 38 (21). https://doi.org/10.1029/2011gl049458. doi: Artn L21404.
Lewis, A.J., 1998. Geomorphic and hydrologic applications of active microwave remote sensing. In: Principles and Applications of Imaging Radar. Manual of Remote Sensing. Wiley, New York, pp. 567–629.
Li, W.Y., Gong, P., 2016. Continuous monitoring of coastline dynamics in western Florida with a 30-year time series of Landsat imagery. Remote Sens. Environ. 179, 196–209. https://doi.org/10.1016/j.rse.2016.03.031.
Li, Y., Piao, S.L., Li, L.Z.X., Chen, A.P., Wang, X.H., Ciais, P., Huang, L., Lian, X., Peng, S.S., Zeng, Z.Z., Wang, K., Zhou, L.M., 2018. Divergent hydrological response to large-scale afforestation and vegetation greening in China. Sci. Adv. 4 (eaar4182). https://doi.org/10.1126/sciadv.aar4182.
Liu, Y., Li, M., Zhou, M., Yang, K., Mao, L., 2013. Quantitative analysis of the waterline method for topographical mapping of tidal flats: a case study in the dongsha sand-bank, China. Remote Sens. 5, 6138–6158. https://doi.org/10.3390/rs5116138.
Liu, J., Kuang, W., Zhang, Z., Xu, X., Qin, Y., Ning, J., Zhou, W., Zhang, S., Li, R., Yan, C., Wu, S., Shi, X., Jiang, N., Yu, D., Pan, X., Chi, W., 2014. Spatiotemporal characteristics, patterns, and causes of land-use changes in China since the late 1980s. J. Geogr. Sci. 24, 195–210. https://doi.org/10.1007/s11442-014-1082-6.
Loveland, T.R., Reed, B.C., Brown, J.F., Ohlen, D.O., Zhu, Z., Yang, L., Merchant, J.W., 2000. Development of a global land cover characteristics database and IGBP DISCover from 1 km AVHRR data. Int. J. Remote Sens. 21, 1303–1330. https://doi.org/10.1080/014311600210191.
Ma, Z., Li, B., 2015. Complex ecology of China's seawall response. Science 347 (1080). https://doi.org/10.1126/science.347.6226.1080-a.
Ma, Z.J., Hua, N., Peng, H.B., Choi, C., Battley, P.F., Zhou, Q.Y., Chen, Y., Ma, Q., Jia, N., Xue, W.J., Bai, Q.Q., Wu, W., Feng, X.S., Tang, C.D., 2013. Differentiating between stopover and staging sites: functions of the southern and northern Yellow Sea for long-distance migratory shorebirds. J. Avian Biol. 44, 504–512. https://doi.org/10.1111/j.1600-048X.2013.00213.x.
Ma, Z.J., Melville, D.S., Liu, J.G., Chen, Y., Yang, H.Y., Ren, W.W., Zhang, Z.W., Piersma, T., Li, B., 2014. Ecosystems management rethinking China's new great wall. Science 346, 912–914. https://doi.org/10.1126/science.1257258.
Mason, D.C., Scott, T.R., Dance, S.L., 2010. Remote sensing of intertidal morphological change in Morecambe Bay, U.K., between 1991 and 2007. Estuar. Coast. Shelf Sci. 87, 487–496. https://doi.org/10.1016/j.ecss.2010.01.015.
Morris, J.T., Sundareshwar, P.V., Nietch, C.T., Kjerfve, B., Cahoon, D.R., 2002. Responses of coastal wetlands to rising sea level. Ecology 83, 2869–2877. https://doi.org/10.2307/3072022.
Murray, N.J., Phinn, S.R., Clemens, R.S., Roelfsema, C.M., Fuller, R.A., 2012. Continental scale mapping of tidal flats across east Asia using the landsat archive. Remote Sens. 4, 3417–3426. https://doi.org/10.3390/rs4113417.
Murray, N.J., Clemens, R.S., Phinn, S.R., Possingham, H.P., Fuller, R.A., 2014. Tracking the rapid loss of tidal wetlands in the Yellow Sea. Front. Ecol. Environ. 12, 267–272. https://doi.org/10.1890/130260.
Niu, Z., Gong, P., Cheng, X., Guo, J., Wang, L., Huang, H., Shen, S., Wu, Y., Wang, X., Wang, X., Ying, Q., Liang, L., Zhang, L., Wang, L., Yao, Q., Yang, Z., Guo, Z., Dai, Y., 2009. Geographical characteristics of China's wetlands derived from remotely sensed data. Sci. China Ser. D Earth Sci. 52, 723–738. https://doi.org/10.1007/s11430-009-0075-2.
Niu, Z.G., Zhang, H.Y., Wang, X.W., Yao, W.B., Zhou, D.M., Zhao, K.Y., Zhao, H., Li, N.N., Huang, H.B., Li, C.C., Yang, J., Liu, C.X., Liu, S., Wang, L., Li, Z., Yang, Z.Z., Qiao, F., Zheng, Y.M., Chen, Y.L., Sheng, Y.W., Gao, X.H., Zhu, W.H., Wang, W.Q., Wang, H., Weng, Y.L., Zhuang, D.F., Liu, J.Y., Luo, Z.C., Cheng, X., Guo, Z.Q., Gong, P., 2012. Mapping wetland changes in China between 1978 and 2008. Chin. Sci. Bull. 57, 2813–2823. https://doi.org/10.1007/s11434-012-5093-3.
Oost, A.P., Hoekstra, P., Wiersma, A., Flemming, B., Lammerts, E.J., Pejrup, M., Hofstede, J., van der Valk, B., Kiden, P., Bartholdy, J., van der Berg, M.W., Vos, P.C., de Vries, S., Wang, Z.B., 2012. Barrier island management: lessons from the past and directions for the future. Ocean Coast. Manag. 68, 18–38. https://doi.org/10.1016/j.ocecoaman.2012.07.010.
Pahlevan, N., Sarkar, S., Franz, B.A., Balasubramanian, S.V., He, J., 2017. Sentinel-2 MultiSpectral Instrument (MSI) data processing for aquatic science applications: demonstrations and validations. Remote Sens. Environ. 201, 47–56. https://doi.org/10.1016/j.rse.2017.08.033.
Pan, B., Mei, H., 2017. Study on the Influence of Water and Sediment in the Yellow River

on the Delta Front. Shandong Normal University, Jinan, China.
Pardo-Pascual, J.E., Almonacid-Caballer, J., Ruiz, L.A., Palomar-Vázquez, J., 2012. Automatic extraction of shorelines from Landsat TM and ETM+ multi-temporal images with subpixel precision. Remote Sens. Environ. 123, 1–11. https://doi.org/10.1016/j.rse.2012.02.024.
Pekel, J.F., Cottam, A., Gorelick, N., Belward, A.S., 2016. High-resolution mapping of global surface water and its long-term changes. Nature 540 (418).
Puliti, S., Saarela, S., Gobakken, T., Ståhl, G., Næsset, E., 2018. Combining UAV and Sentinel-2 auxiliary data for forest growing stock volume estimation through hierarchical model-based inference. Remote Sens. Environ. 204, 485–497. https://doi.org/10.1016/j.rse.2017.10.007.
Reiche, J., Hamunyela, E., Verbesselt, J., Hoekman, D., Herold, M., 2018. Improving near-real time deforestation monitoring in tropical dry forests by combining dense Sentinel-1 time series with Landsat and ALOS-2 PALSAR-2. Remote Sens. Environ. 204, 147–161. https://doi.org/10.1016/j.rse.2017.10.034.
Rodriguez, J.F., Saco, P.M., Sandi, S., Saintilan, N., Riccardi, G., 2017. Potential increase in coastal wetland vulnerability to sea-level rise suggested by considering hydrodynamic attenuation effects. Nat. Commun. 8 (16094). https://doi.org/10.1038/ncomms16094. doi:ARTN 16094.
Ryu, J.H., Won, J.S., Min, K.D., 2002. Waterline extraction from Landsat TM data in a tidal flat - a case study in Gomso Bay, Korea. Remote Sens. Environ. 83, 442–456. https://doi.org/10.1016/s0034-4257(02)00059-7.
Sagar, S., Roberts, D., Bala, B., Lymburner, L., 2017. Extracting the intertidal extent and topography of the Australian coastline from a 28 year time series of Landsat observations. Remote Sens. Environ. 195, 153–169. https://doi.org/10.1016/j.rse.2017.04.009.
Santoro, M., Wegmueller, U., Lamarche, C., Bontemps, S., Defoumy, P., Arino, O., 2015. Strengths and weaknesses of multi-year Envisat ASAR backscatter measurements to map permanent open water bodies at global scale. Remote Sens. Environ. 171, 185–201. https://doi.org/10.1016/j.rse.2015.10.031.
Syvitski, J.P.M., Vorosmarty, C.J., Kettner, A.J., Green, P., 2005. Impact of humans on the flux of terrestrial sediment to the global coastal ocean. Science 308, 376–380. https://doi.org/10.1126/science.1109454.
Tseng, K.H., Kuo, C.Y., Lin, T.H., Huang, Z.C., Lin, Y.C., Liao, W.H., Chen, C.F., 2017. Reconstruction of time-varying tidal flat topography using optical remote sensing imageries. ISPRS J. Photogramm. Remote Sens. 131, 92–103. https://doi.org/10.1016/j.isprsjprs.2017.07.008.
Tucker, C.J., 1979. Red and photographic infrared linear combinations for monitoring vegetation. Remote Sens. Environ. 8, 127–150. https://doi.org/10.1016/0034-4257(79)90013-0.
Veloso, A., Mermoz, S., Bouvet, A., Le Toan, T., Planells, M., Dejoux, J.F., Ceschia, E., 2017. Understanding the temporal behavior of crops using Sentinel-1 and Sentinel-2-like data for agricultural applications. Remote Sens. Environ. 199, 415–426. https://doi.org/10.1016/j.rse.2017.07.015.
Wang, J., Niu, Z., 2017. Remote-sensing analysis of Yancheng intertidal zones based on tidal correction. Haiyang Xuebao. 39, 149–160. https://doi.org/10.3969/j.issn.0253-4193.2017.05.014.
Wang, H.J., Yang, Z.S., Saito, Y., Liu, J.P., Sun, X.X., Wang, Y., 2007. Stepwise decreases of the Huanghe (Yellow River) sediment load (1950–2005): impacts of climate change and human activities. Glob. Planet. Chang. 57, 331–354. https://doi.org/10.1016/j.gloplacha.2007.01.003.
Wang, S., Fu, B., Piao, S., Lu, Y., Ciais, P., Feng, X., Wang, Y., 2016. Reduced sediment transport in the Yellow River due to anthropogenic changes. Nat. Geosci. 9 (38). https://doi.org/10.1038/ngeo2602.
Wei, W., Tang, Z., Dai, Z., Lin, Y., Ge, Z., Gao, J., 2015. Variations in tidal flats of the Changjiang (Yangtze) estuary during 1950s–2010s: future crisis and policy implication. Ocean Coast. Manag. 108, 89–96. https://doi.org/10.1016/j.ocecoaman.2014.05.018.
White, S.M., Madsen, E.A., 2016. Tracking tidal inundation in a coastal salt marsh with Helikite airphotos: influence of hydrology on ecological zonation at Crab Haul Creek, South Carolina. Remote Sens. Environ. 184, 605–614. https://doi.org/10.1016/j.rse.2016.08.005.
Wilson, H.B., Kendall, B.E., Fuller, R.A., Milton, D.A., Possingham, H.P., 2011. Analyzing variability and the rate of decline of migratory shorebirds in Moreton Bay, Australia. Conserv. Biol. 25, 758–766. https://doi.org/10.1111/j.1523-1739.2011.01670.x.
Wu, X., Bi, N.S., Xu, J.P., Nittrouer, J.A., Yang, Z.S., Saito, Y., Wang, H.J., 2017. Stepwise morphological evolution of the active Yellow River (Huanghe) delta lobe (1976–2013): dominant roles of riverine discharge and sediment grain size. Geomorphology 292, 115–127. https://doi.org/10.1016/j.geomorph.2017.04.042.
Xiao, X., 2004. Modeling gross primary production of temperate deciduous broadleaf forest using satellite images and climate data. Remote Sens. Environ. 91, 256–270. https://doi.org/10.1016/j.rse.2004.03.010.
Xiao, X.M., Braswell, B., Zhang, Q.Y., Boles, S., Frolking, S., Moore, B., 2003. Sensitivity of vegetation indices to atmospheric aerosols: continental-scale observations in Northern Asia. Remote Sens. Environ. 84, 385–392. https://doi.org/10.1016/s0034-4257(02)00129-3.
Xiao, X.M., Boles, S., Frolking, S., Li, C.S., Babu, J.Y., Salas, W., Moore, B., 2006. Mapping paddy rice agriculture in South and Southeast Asia using multi-temporal MODIS images. Remote Sens. Environ. 100, 95–113. https://doi.org/10.1016/j.rse.2005.10.004.
Xiao, X., Biradar, C.M., Czarnecki, C., Alabi, T., Keller, M., 2009. A simple algorithm for large-scale mapping of evergreen forests in tropical America, Africa and Asia. Remote Sens. 1, 355–374. https://doi.org/10.3390/rs1030355.
Xu, H.Q., 2006. Modification of normalised difference water index (NDWI) to enhance open water features in remotely sensed imagery. Int. J. Remote Sens. 27, 3025–3033. https://doi.org/10.1080/01431160600589179.
Yao, H., 2013. Characterizing landuse changes in 1990–2010 in the coastal zone of Nantong, Jiangsu province, China. Ocean Coast. Manag. 71, 108–115. https://doi.org/10.1016/j.ocecoaman.2012.09.007.
Zahran, S., Brody, S.D., Grover, H., Vedlitz, A., 2006. Climate change vulnerability and policy support. Soc. Nat. Resour. 19, 771–789. https://doi.org/10.1080/08941920600835528.
Zhang, G.L., Xiao, X.M., Dong, J.W., Kou, W.L., Jin, C., Qin, Y.W., Zhou, Y.T., Wang, J., Menarguez, M.A., Biradar, C., 2015a. Mapping paddy rice planting areas through time series analysis of MODIS land surface temperature and vegetation index data. ISPRS J. Photogramm. Remote Sens. 106, 157–171. https://doi.org/10.1016/j.isprsjprs.2015.05.011.
Zhang, Y.C., Ma, R.H., Zhang, M., Duan, H.T., Loiselle, S., Xu, J.D., 2015b. Fourteen-year record (2000−2013) of the spatial and temporal dynamics of floating algae blooms in Lake Chaohu, observed from time series of MODIS images. Remote Sens. 7, 10523–10542. https://doi.org/10.3390/rs70810523.
Zhang, G.L., Xiao, X.M., Biradar, C.M., Dong, J.W., Qin, Y.W., Menarguez, M.A., Zhou, Y.T., Zhang, Y., Jin, C., Wang, J., Doughty, R.B., Ding, M.J., Moore, B., 2017. Spatiotemporal patterns of paddy rice croplands in China and India from 2000 to 2015. Sci. Total Environ. 579, 82–92. https://doi.org/10.1016/j.scitotenv.2016.10.223.
Zhang, S.L., Yang, D.W., Yang, Y.T., Piao, S.L., Yang, H.B., Lei, H.M., Fu, B.J., 2018. Excessive Afforestation and Soil Drying on China's Loess Plateau. J. Geophys. Res. 123, 923–935. https://doi.org/10.1002/2017jg004038.
Zhao, B., Guo, H., Yan, Y., Wang, Q., Li, B., 2008. A simple waterline approach for tidelands using multi-temporal satellite images: a case study in the Yangtze Delta. Estuar. Coast. Shelf Sci. 77, 134–142. https://doi.org/10.1016/j.ecss.2007.09.022.
Zhao, Y.F., Zou, X.Q., Liu, Q., Yao, Y.L., Li, Y.L., Wu, X.W., Wang, C.L., Yu, W.W., Wang, T., 2017. Assessing natural and anthropogenic influences on water discharge and sediment load in the Yangtze River, China. Sci. Total Environ. 607, 920–932. https://doi.org/10.1016/j.scitotenv.2017.07.002.
Zheng, K., Zheng, Y., Gao, L., Gao, R., 2012. Experiment process and effect of the artificial water supplement for the Diaokouhe River in the Yellow River Delta during 2010–2011. Water Conserv. Sci. Technol. Econ. 18, 12–15.
Zhou, Y., Dong, J., Xiao, X., Xiao, T., Yang, Z., Zhao, G., Zou, Z., Qin, Y., 2017. Open surface water mapping algorithms: a comparison of water-related spectral indices and sensors. WaterSA 9 (256). https://doi.org/10.3390/w9040256.
Zhu, Z., Woodcock, C.E., 2012. Object-based cloud and cloud shadow detection in Landsat imagery. Remote Sens. Environ. 118, 83–94. https://doi.org/10.1016/j.rse.2011.10.028.
Zhu, Z., Wang, S., Woodcock, C.E., 2015. Improvement and expansion of the Fmask algorithm: cloud, cloud shadow, and snow detection for Landsats 4–7, 8, and Sentinel 2 images. Remote Sens. Environ. 159, 269–277. https://doi.org/10.1016/j.rse.2014.12.014.
Zou, Z.H., Dong, J.W., Menarguez, M.A., Xiao, X.M., Qin, Y.W., Doughty, R.B., Hooker, K.V., Hambright, K.D., 2017. Continued decrease of open surface water body area in Oklahoma during 1984–2015. Sci. Total Environ. 595, 451–460. https://doi.org/10.1016/j.scitotenv.2017.03.259.
Zou, Z.H., Xiao, X.M., Dong, J.W., Qin, Y.W., Doughty, R.B., Menarguez, M.A., Zhang, G.L., Wang, J., 2018. Divergent trends of open-surface water body area in the contiguous United States from 1984 to 2016. Proc. Natl. Acad. Sci. U. S. A. 115, 3810–3815. https://doi.org/10.1073/pnas.1719275115.